Euclid: ERO - NISP-only sources and the search for luminous $z = 6$-8 galaxies

J. R. Weaver, S. Taamoli, C. J. R. Mcpartland, L. Zalesky, N. Allen, S. Toft, D. B. Sanders, H. Atek, R. A. A. Bowler, D. Stern, et al.

Astronomy & Astrophysics manuscript no. main
May 24, 2024

Euclid: Early Release Observations – NISP-only sources and the search for luminous $z = 6-8$ galaxies⋆

J. R. Weaver⋆⋆[1], S. Taamoli[2], C. J. R. McPartland[3,4], L. Zalesky[5], N. Allen[6], S. Toft[6,4], D. B. Sanders[5], H. Atek[7], R. A. A. Bowler[8], D. Stern[9], C. J. Conselice[8], B. Mobasher[2], I. Szapudi[5], P. R. M. Eisenhardt[9], G. Murphree[5], I. Valdes[5], K. Ito[10], S. Belladitta[11,12], P. A. Oesch[13,4,6], S. Serjeant[14], D. J. Mortlock[15,16], N. A. Hatch[17], M. Kluge[18], B. Milvang-Jensen[6,4,3], G. Rodighiero[19,20], E. Bañados[11], J. M. Diego[21], R. Gavazzi[22,7], G. Congedo[23], M. Shuntov[24,3,4], H. Dole[25], P.-F. Rocci[25], T. Saifollahi[26,27], M. Miluzio[28,29], M. Ezziati[22], A. C. N. Hughes[15], J.-C. Cuillandre[30], R. Laureijs[31], S. Paltani[13], M. Schirmer[11], C. Stone[32], N. Aghanim[25], B. Altieri[28], A. Amara[33], S. Andreon[34], N. Auricchio[12], M. Baldi[35,12,36], A. Balestra[20], S. Bardelli[12], R. Bender[18,37], C. Bodendorf[18], D. Bonino[38], E. Branchini[39,40,34], M. Brescia[41,42,43], J. Brinchmann[44,45], S. Camera[46,47,38], V. Capobianco[38], C. Carbone[48], V. F. Cardone[49,50], J. Carretero[51,52], S. Casas[53], F. J. Castander[54,55], M. Castellano[49], S. Cavuoti[42,43], A. Cimatti[56], L. Conversi[57,28], Y. Copin[58], L. Corcione[38], F. Courbin[59], H. M. Courtois[60], A. Da Silva[61,62], H. Degaudenzi[13], A. M. Di Giorgio[63], J. Dinis[61,62], M. Douspis[25], F. Dubath[13], X. Dupac[28], A. Ealet[58], M. Farina[63], S. Farrens[30], S. Ferriol[58], S. Fotopoulou[64], M. Frailis[65], E. Franceschi[12], P. Franzetti[48], S. Galeotta[65], W. Gillard[66], B. Gillis[23], C. Giocoli[12,67], P. Gómez-Alvarez[68,28], A. Grazian[20], F. Grupp[18,37], L. Guzzo[69,34], S. V. H. Haugan[70], J. Hoar[28], H. Hoekstra[71], W. Holmes[9], I. Hook[72], F. Hormuth[73], A. Hornstrup[74,3], P. Hudelot[7], K. Jahnke[11], M. Jhabvala[75], E. Keihänen[76], S. Kermiche[66], A. Kiessling[9], T. Kitching[77], B. Kubik[58], M. Kümmel[37], M. Kunz[78], H. Kurki-Suonio[79,80], O. Lahav[81], D. Le Mignant[22], S. Ligori[38], P. B. Lilje[70], V. Lindholm[79,80], I. Lloro[82], D. Maino[69,48,83], E. Maiorano[12], O. Mansutti[65], O. Marggraf[84], K. Markovic[9], N. Martinet[22], F. Marulli[85,12,36], R. Massey[86], D. C. Masters[87], S. Maurogordato[88], H. J. McCracken[7], E. Medinaceli[12], S. Mei[89], M. Melchior[90], Y. Mellier[24,7], M. Meneghetti[12,36], E. Merlin[49], G. Meylan[59], J. J. Mohr[37,18], M. Moresco[85,12], L. Moscardini[85,12,36], R. Nakajima[84], R. C. Nichol[33], S.-M. Niemi[31], C. Padilla[91], F. Pasian[65], K. Pedersen[92], W. J. Percival[93,94,95], V. Pettorino[31], S. Pires[30], G. Polenta[96], M. Poncet[97], L. A. Popa[98], L. Pozzetti[12], F. Raison[18], A. Renzi[19,99], J. Rhodes[9], G. Riccio[42], E. Romelli[65], M. Roncarelli[12], E. Rossetti[35], R. Saglia[37,18], D. Sapone[100], P. Schneider[84], T. Schrabback[101], A. Secroun[66], G. Seidel[11], S. Serrano[55,102,54], C. Sirignano[19,99], G. Sirri[36], L. Stanco[99], P. Tallada-Crespí[51,52], A. N. Taylor[23], H. I. Teplitz[87], I. Tereno[61,103], R. Toledo-Moreo[104], I. Tutusaus[105], L. Valenziano[12,106], T. Vassallo[37,65], A. Veropalumbo[34,40,107], Y. Wang[87], J. Weller[37,18], E. Zucca[12], C. Burigana[108,106], G. Castignani[12], Z. Sakr[109,105,110], V. Scottez[24,111], M. Viel[112,65,113,114,115], P. Simon[84], J. Martín-Fleitas[116], and D. Scott[117]

(Affiliations can be found after the references)

May 24, 2024

ABSTRACT

This paper presents a search for high redshift galaxies from the *Euclid* Early Release Observations program "Magnifying Lens." The 1.5 deg^2 area covered by the twin Abell lensing cluster fields is comparable in size to the few other deep near-infrared surveys such as COSMOS, and so provides an opportunity to significantly increase known samples of rare UV-bright galaxies at $z \approx 6$–8 ($M_{\rm UV} \lesssim -22$). Beyond their still uncertain role in reionisation, these UV-bright galaxies are ideal laboratories from which to study galaxy formation and constrain the bright-end of the UV luminosity function. Of the 501 994 sources detected from a combined $Y_{\rm E}$, $J_{\rm E}$, and $H_{\rm E}$ NISP detection image, 168 do not have any appreciable VIS/$I_{\rm E}$ flux. These objects span a range in spectral colours, separated into two classes: 139 extremely red sources; and 29 Lyman-break galaxy candidates. Best-fit redshifts and spectral templates suggest the former is composed of both $z \gtrsim 5$ dusty star-forming galaxies and $z \approx 1$–3 quiescent systems. The latter is composed of more homogeneous Lyman break galaxies at $z \approx 6$–8. In both cases, contamination by L- and T-type dwarfs cannot be ruled out with *Euclid* images alone. Additional contamination from instrumental persistence is investigated using a novel time series analysis. This work lays the foundation for future searches within the Euclid Deep Fields, where thousands more $z \gtrsim 6$ Lyman break systems and extremely red sources will be identified.

Key words. Galaxies: high-redshift; Galaxies: evolution; Catalogues

⋆ This paper is published on behalf of the Euclid Consortium
⋆⋆ e-mail: jweaver@astro.umass.edu

1. Introduction

The reionisation of neutral hydrogen within the intergalactic medium (IGM) marks a major transition in cosmic history. Ionising Lyman continuum photons emitted from the first generations of massive stars is thought to have contributed significantly to the reionization budget (Dayal & Ferrara 2018; Finkelstein et al. 2019; Atek et al. 2024b). Observations from *Planck* find $z = 7.67 \pm 0.73$ as the mid-point of the reionization era, concluding sometime around $z \approx 6$ with a transparent IGM (Planck Collaboration et al. 2016). Within the standard paradigm of hierarchical structure formation, the first structures collapse within the most overdense regions of the primordial web of dark matter (White & Frenk 1991; Behroozi et al. 2019), from which the first stars form. As such, the topology of reionisation should be patchy, varying significantly over degree scales (Trac et al. 2015; Neyer et al. 2023; Lu et al. 2024). Galaxies born out of these overdensities are expected to be rapidly star-forming and therefore UV luminous, but correspondingly rare (Kauffmann et al. 2022; Naidu et al. 2022b). Elsewhere, collections of less UV luminous systems formed in comparably greater numbers (Bouwens et al. 2015; Finkelstein et al. 2015; Qin et al. 2019; Kauffmann et al. 2022; Bouwens et al. 2023; Leung et al. 2023; Adams et al. 2024; Donnan et al. 2024). Recent advancements enabled by the *James Webb* Space Telescope (JWST) suggest that while the total ionising flux of UV luminous galaxies is higher, the escape fraction of ionising photons and therefore relative ionising contribution may be subdominant (Roberts-Borsani et al. 2023; Endsley et al. 2023; Atek et al. 2024b). Furthermore, the discovery of surprisingly massive active black holes at $z \approx 6$–10 has re-ignited the possibility of a quasar contribution to reionisation (Bañados et al. 2018; Furtak et al. 2023; Juodžbalis et al. 2023; Kokorev et al. 2023; Dayal et al. 2024; Greene et al. 2024).

Owing to their apparent magnitudes $J \approx 24$–26 AB and observational accessibility from near-infrared (NIR) surveys, UV luminous galaxies ($M_{\rm UV} \lesssim -21$ AB) from the reionization era ($z > 6$) have been detected from the few degree-scale NIR surveys wide enough to find them, e.g., SXDF and COSMOS (Bowler et al. 2014; Kauffmann et al. 2022; Donnan et al. 2023; Varadaraj et al. 2023). Pre-JWST studies already hinted at a potential excess of UV-luminous galaxies at $z = 8$–10 compared to typically assumed Schechter functional forms, and a seemingly slow evolution in the bright-end of the galaxy UV luminosity function at these redshifts (Bowler et al. 2020). This slow evolution in the number density of UV-bright galaxies is being confirmed by the most recent observations of JWST at $z > 10$ (e.g. Harikane et al. 2023; Chemerynska et al. 2023; Adams et al. 2024). However, their scarce number density on the sky makes it challenging to assemble large samples to accurately determine the shape of bright end of the UV luminosity function, which holds crucial information on the early assembly of galaxies. Neither the *Hubble* Space Telescope (HST) nor JWST are capable of efficiently surveying degree-scale areas, requiring continued investment in large (albeit lower resolution) NIR surveys from space and the ground.

These UV luminous, rapidly star forming galaxies are expected to be some of the fastest growing systems of their epoch. Although speculative in nature, they are some of the most suitable candidates for being the progenitors of massive galaxies at later epochs, possibly also of the first generation to have ceased star-formation (Carnall et al. 2023; Glazebrook et al. 2023). If so, then these rare systems are vital laboratories for examining galaxy evolution at its most extreme. Constraining their mass build up and future evolution requires star formation rates, stellar masses, star-formation histories, and estimates of their gas resevoirs. Detailed spectroscopic follow-up is only now beginning to reveal the extraordinary variation in their physical properties (Endsley et al. 2022; Bowler et al. 2024; Algera et al. 2024; Schouws et al. 2023). Given this diversity, the limited samples currently available from the few degree-scale deep NIR surveys are insufficient to characterise them as a population. Progress as to their nature and contribution to reionisation requires even larger NIR surveys.

Another major contribution from NIR surveys is the discovery of extremely red sources (e.g., Wang et al. 2016; Franco et al. 2018; Wang et al. 2019; Zavala et al. 2021). Presumably reddened by dust obscuration, far-infrared studies have accomplished much by identifying the UV light reprocessed by obscuring dust clouds. JWST too, in its first images, revealed a surprising abundance of extremely red, dust-obscured disc galaxies (Nelson et al. 2023), which may have significant contributions to the stellar mass and star-formation budgets at $z > 3$ (Gottumukkala et al. 2024; Wang et al. 2024; Williams et al. 2023). However, quiescent galaxies with their characteristically old stellar populations are a known but important interloper population (Barrufet et al. 2024). Both pose significant obstacles to identifying genuine high-redshift galaxies (Naidu et al. 2022a; Zavala et al. 2023).

The European Space Agency (ESA) *Euclid* mission was launched in July 2023. A medium-class probe, it was designed to survey the Universe to uncover details as to the nature and evolution of dark matter and dark energy – two elusive components of the ΛCDM cosmological model (Laureijs et al. 2011; Euclid Collaboration: Mellier et al. 2024). Its two instruments are the visible instrument (VIS, Euclid Collaboration: Cropper et al. 2024) with its characteristic ultra-broad $I_{\rm E}$ passband ideally suited for obtaining high-resolution optical imaging necessary for weak lensing studies, and the Near-Infrared Spectrometer and Photometer (NISP, Euclid Collaboration: Jahnke et al. 2024), providing a complement of lower-resolution NIR data in the $Y_{\rm E}$, $J_{\rm E}$, and $H_{\rm E}$ passbands (Euclid Collaboration: Schirmer et al. 2022) to secure photometric redshifts in addition to slitless grism spectroscopy. This unique combination of instruments is key to achieving *Euclid*'s objectives, and goes hand-in-hand with the multi-tiered survey strategy ranging from the Euclid Wide Survey (EWS, Euclid Collaboration: Scaramella et al. 2022) over 14 000 deg^2 to a 53 deg^2 Euclid Deep Survey (EDS) of three primary fields: the Euclid Deep Field North (EDF-North); the Euclid Deep Field South (EDF-South); and the Euclid Deep Field Fornax (EDF-Fornax). Additional complements from well-studied auxiliary fields, such as COSMOS and a self-calibration field within EDF-North, along with grism observations, are purposely designed to improve key measurements.

Six Early Release Observations (ERO) projects were chosen to highlight the capability of *Euclid* to study a variety of astrophysical phenomena (Cuillandre et al. 2024; Euclid Early Release Observations 2024). Among them, "Magnifying Lens" (PI: H. Atek) takes aim at two massive galaxy clusters, Abell 2390 and Abell 2764, with VIS/$I_{\rm E}$, NISP/$Y_{\rm E}$, $J_{\rm E}$, $H_{\rm E}$, as well as NISP grism observations (Atek et al. 2024a). While the magnifying power of their deep gravitational potentials helps to resolve galaxies immediately behind the cluster, the large 0.75 deg^2 area of each field enables an order-of-magnitude increase in the number of detectable $z \gtrsim 6$ UV bright galaxies compared to small area blank fields from HST and JWST (e.g., CANDELS, Duncan et al. 2014; Bouwens et al. 2015; Finkelstein et al. 2015). This rich sample of high-redshift systems can then be used to constrain the UV luminosity functions of galaxies and quasars,

the physics of which can be studied from detailed spectroscopic follow up. These same observations can also be used to constrain dark matter through weak lensing analyses, as well as the virial masses and assembly history of the cluster galaxies themselves.

This work aims to showcase the ability of *Euclid* to identify rare NISP-only objects (i.e., not detected in VIS/I_E), such as luminous high-redshift galaxies and extremely red sources, and is organised as follows. Section 2 describes the observations, data reduction, and photometric catalogue of Abell 2390 and Abell 2764. Section 3 presents the methodology adopted to identify NISP-only objects. Section 4 presents the photometrically-selected sample, its properties, sources of potential contamination, and physical interpretation. Section 5 discusses the challenges encountered and a prospectus for identifying such systems from the EDS and auxiliary fields. These results are computed adopting a standard ΛCDM cosmology with $H_0 = 70\,\mathrm{km\,s^{-1}\,Mpc^{-1}}$, $\Omega_m = 0.3$ and $\Omega_\Lambda = 0.7$ throughout. All magnitudes are expressed in the AB system (Oke 1974), for which a flux f_ν in μJy (10^{-29} erg cm^{-2}s^{-1}Hz^{-1}) corresponds to an AB magnitude of $23.9 - 2.5\,\log_{10}(f_\nu/\mu\mathrm{Jy})$.

2. Data and photometric catalogue

2.1. Observations

The ERO "Magnifying Lens" project consists of intermediate-depth observations of two known galaxy clusters, Abell 2390 and Abell 2764. While both are rich systems with many lensed background sources, Abell 2390 ($z = 0.228$, Sohn et al. 2020) is better studied than Abell 2764 ($z = 0.07$, Katgert et al. 1996). See Atek et al. (2024a) for details of the field selection.

For each cluster, *Euclid* obtained three reference observing sequences (ROS, see Fig. 8 of Euclid Collaboration: Scaramella et al. 2022) of 70.2 min which include VIS/I_E and NISP/Y_E, J_E, H_E imaging, adopting a 3′×3′ dither between each ROS to fill-in coverage between the 36 chips. Individual I_E, Y_E, J_E, and H_E exposures were stacked to produce four deep mosaics using `SWarp` (Bertin et al. 2002) at native 0.″1 pix^{-1} and 0.″3 pix^{-1} scales, respectively. A 64 pixel mesh and 3× smoothing factor was adopted to model and subtract the background light, which for VIS is more challenging given the bluer Galactic cirrus foreground. Although other images produced through other approaches were considered, this work adopts the "Compact-sources" images because they are optimised for photometry of faint, compact objects. See Cuillandre et al. (2024) for a complete description of the reduction procedure.

Each mosaic spans 0.75 deg^2, making the $I_E = 27.1$ AB (5σ point source) VIS images some of the deepest at such high-resolution covering degree-scales, comparable only to the largest HST mosaic taken (ACS/F814W over 1.7 deg^2 in COSMOS, Koekemoer et al. 2011). Similarly, the Y_E, J_E, and H_E ≈24.5 AB (5σ point source) images are some of the deepest NIR imaging covering degree-scales, comparable only to VIDEO (Jarvis et al. 2013) and the UltraVISTA survey of COSMOS (McCracken et al. 2012). Although designed for identifying new strongly lensed galaxies, their large contiguous areas beyond the cluster centres make them well-suited for identifying high-redshift, rest-frame UV bright objects that are too rare to be found consistently by smaller NIR surveys.

2.2. Photometric catalogue

Sources were detected in each field using Pythonic Source Extractor (`SEP`, Bertin & Arnouts 1996; Barbary 2016) from a `CHI_MEAN` coadd of all three NISP Y_E, J_E, and H_E mosaics constructed using `SWarp` (Bertin et al. 2002). To achieve maximal completeness, `SEP` was configured to detect sources whose pixels are significant above $1.5\,\sigma$ across at least three contiguous pixels after smoothing with a 0.″45 (1.5 pixel) full-width-half-maximum Gaussian kernel (see Euclid Collaboration: Zalesky et al. 2024 for relevant discussion). Aggressive deblending is crucial to separating the relatively low-resolution NISP-only sources from line-of-sight neighbours. As such, `SEP` is configured to deblend with 2×10^5 thresholds, requiring a contrast of 10^{-5}, tuned by visual inspection. Cleaning was not applied as it is liable to remove real sources of interest. A total of 501 994 sources were recovered (98% have S/N > 3 in either Y_E, J_E, or H_E) with approximately equal numbers in each 0.5 deg^2 field: 252 675 in Abell 2390; and 249 319 in Abell 2764.

Photometry was measured at source positions in circular apertures with diameters of 0.″1, 0.″2, 0.″3, 0.″6, 1.″0, 1.″2, 1.″5, and 2.″0. Uncertainties were measured similarly on the weight maps; their effective per-pixel error distributions were verified to be consistent with the per-pixel noise estimated directly from the science mosaics. Given the 0.″3 pix^{-1} scale of NISP, aperture diameters below 0.″6 are generally only suitable for VIS photometry.

Considering the difference in resolution and spatial sampling between VIS and NISP, it would seem advantageous to convolve all of the images to the broadest PSF, which is H_E. However, this work exploits the unique potential of using VIS solely as a "dropout" band where the colour terms between I_E and Y_E, J_E, and H_E are largely inconsequential relative to the much more important signal-to-noise ratio (S/N) estimate from VIS/I_E which would be severely degraded if the image were downsampled and smoothed. Instead, the VIS/I_E S/N can be optimally determined from the original high-resolution images using a suitably chosen aperture that is large enough to be robust to noise but not corrupted by neighbouring sources. This fact, together with the relatively similar PSFs between all three NISP bands and the expected compactness of high-redshift Lyman break galaxies (<1″in radius, e.g., Bowler et al. 2017) means that we can expect to produce high-fidelity NISP colours by simply assuming that any light outside the aperture of choice is explained by the PSF.

All aperture flux estimates and their uncertainties are corrected to total flux by dividing by the fractional energy outside each aperture. This extended light distribution is measured from observed PSFs constructed by optimally stacking recentred cutouts of point sources identified from the science mosaics following Weaver et al. (2024). Relevant multiplicative correction factors for VIS are 16×, 3×, and 2× for 0.″1, 0.″2, and 0.″3 diameters, respectively; and 1.2×, 1.3×, and for NISP are 1.4× for 1.″2 diameter apertures in Y_E, J_E, and H_E, respectively.

To facilitate community engagement with these ERO data, a combined photometric catalogue of all 501 994 sources is released with this work, jointly with the overview paper of Atek et al. (2024a). The catalogue includes unique source identification numbers and field-specific identifiers, sky coordinates, elementary shape estimates, aperture and total fluxes, flux errors, and their aperture-to-total corrections, in addition to `Source Extractor`-like flags. Photometry is provided already corrected for Galactic extinction mapped by Schlafly & Finkbeiner (2011), adopting the extinction curves of Fitzpatrick & Massa (2007). There is a large number of artefacts near the mosaic edges where only a single dither contributes, as well as along the diffraction spikes of bright stars; these sources are identified in a hand-built region mask that excludes 15%

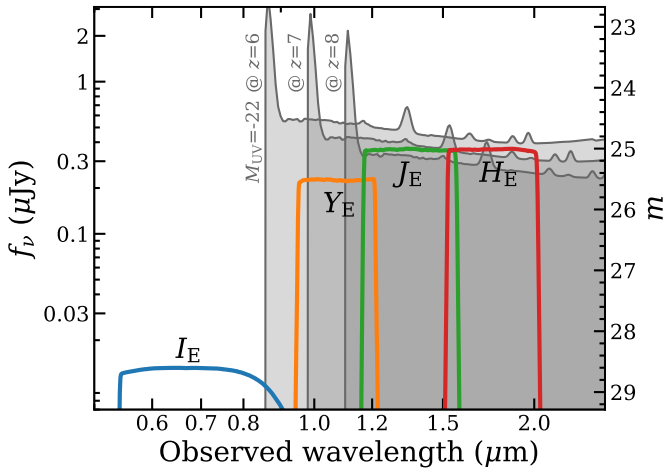

Fig. 1: Summary of *Euclid*'s ability to identify bright $M_{UV} < -22$ LBGs detectable only in NISP (or VIS/I_E "dropout") from the ERO data of Abell 2764 and Abell 2390. Model spectra of an LBG at $z = 7$, 8, and 9 are generated with `python-FSPS`. *Euclid* I_E, Y_E, J_E, and H_E transmission curves are normalised such that their peak coincides with the selection function adopted in this work.

of the total catalogue (`use_phot` = 0) near bright stars, diffraction spikes, and approximately 1′ around the mosaic edge. For the complete details, consult the `README` document provided with the catalogue at https://zenodo.org/doi/10.5281/zenodo.11151975.

3. Candidate identification

Rather than only identifying galaxies at $z \approx 6$–8, this work aims to identify all systems that are found only in the NISP Y_E, J_E, and H_E bands, lacking any detectable VIS I_E signal. As such, a selection function is adopted requiring a S/N < 1.5 for VIS/I_E ($\approx$ 28.5 total) in each of 0.″1, 0.″2, and 0.″3 diameter apertures. While this unusually strict criterion can reject some real $z \approx 6$–7 sources with non-negligible ionising UV continuum flux blueward of Lyα, it is necessary in order to maximise reliability (future ancillary optical data will help to relax this). Furthermore, sources are required to have J_E and H_E < 25 (S/N $\gtrsim$ 5) and Y_E < 25.5 (S/N $\gtrsim$ 3), all total magnitudes, relaxing the latter condition to allow for $z \approx 8$ solutions where the Lyman break is only marginally observed, but limits the search to $z \lesssim 8.5$. However, the criteria demand that even the faintest candidates have an extraordinarily strong break with $I_E - Y_E > 2$ AB, greater than most Lyman-break selection criteria used in HST and JWST surveys (e.g., Bouwens et al. 2015; Finkelstein et al. 2015; Atek et al. 2024b; Adams et al. 2024), making these candidates unusually secure. Figure 1 illustrates these criteria relative to an $M_{UV} = -22$ LBG at $z = 7$, 8, and 9 built from `Python-FSPS` (Conroy et al. 2009; Conroy & Gunn 2010; Johnson et al. 2023); this is a simple toy model assuming a maximally opaque foreground IGM, high Lyα escape, and no damping wing. The height of each transmission curve is set to the effective depth of this selection function.

For NISP, larger 1.″2 diameter apertures are chosen because they will enclose marginally resolved features expected of $z \approx 6$–9 LBGs (e.g., Bowler et al. 2017). All colours are computed using the total fluxes because they produce less biased colours compared to aperture fluxes alone. To safeguard against artefacts near edges and diffraction spikes, sources in the masked regions are discounted. Furthermore, extremely extended sources unlikely to be high redshift are rejected by requiring that H_E fluxes in 2.″0 apertures contain less than 20% more light than is contained in 1.″5 diameter apertures. Of the total 262 sources satisfying these criteria, a visual inspection identified 66 likely artefacts and 27 VIS detections arising from occasional unmasked anomalies in the mosaics, e.g., diffraction spikes, cosmic rays, and low exposure areas.

Figure 2 and Fig. 3 illustrate the colours and compactness of the 168 remaining candidates. Interestingly, despite overall similar detections in each field, 109 sources are found in Abell 2390 and only 59 in Abell 2764, a ratio of about 2 to 1. Reasons for this are likely related to brown dwarfs from the Galaxy, since the two fields have very different Galactic latitudes (see Sect. 5).

4. Results

The 168 sources selected in this work represent the most robust NISP-only objects chosen from Abell 2390 and Abell 2764. It is neither a complete sample nor a pure one, but is intended to showcase the potential of *Euclid* and its ability to select promising high-redshift galaxies, among other interesting NISP-only sources.

4.1. Properties of robust NISP-only sources

The candidates span a remarkable range in colour from extremely red to relatively flat colours. Figure 2 provides an overview of the properties of the sample. To better contrast this diversity, we elect to refer to the redder subsample of 129 VIS-undetected objects as "extremely red sources" (ERSs), defined as having robustly red $J_E - H_E$ and $Y_E - J_E$ colours, whereby a flat f_ν spectrum cannot be supported within the 1σ flux uncertainties of either colour. As evidenced by the reddening vector, these objects are consistent with high dust obscuration, although quiescent solutions are also possible (see Sect. 5). The remaining 29 objects with flat f_ν colours in both $J_E - H_E$ and $Y_E - J_E$ are then consistent with $z \approx 6$–9 LBGs, as demonstrated by the grid of redshifts and mean stellar ages (10, 50, and 100 Myr) derived from simple single stellar population models built with `Python-FSPS` including nebular emission line contributions. It is worth noting that although selected by consideration of their flux uncertainties, the two samples are clearly distinguished by their expected colours alone. Given that precise calibration of *Euclid* is ongoing (although zero-point uncertainties are likely already below 0.1), this work purposely avoids defining a strict colour-colour selection for either category. Summary information of the LBG and ERS candidates are listed in Table A.1 and Table B.1–B.4, respectively.

Morphologically, the majority of ERSs are at least marginally resolved or even disc-like whereas the LBGs occupy a range in compactness estimated from H_E flux ratios between 1.″5 and 2.″0 diameter apertures, as shown in Fig. 2c. While the faintest LBGs appear more compact than point sources which have a typical flux ratio $\approx$ 1.0–1.1, they are likely unresolved objects whose flux ratio estimate is driven by noise. Visual inspection confirms this picture. Furthermore, only a few sources are close enough to the cluster core where magnification could be appreciable, which is particularly important for estimates of rest-frame UV magnitudes for the LBG candidates. Cutouts of all 168 sources, including false-colour images, are presented in Appendices A and B.

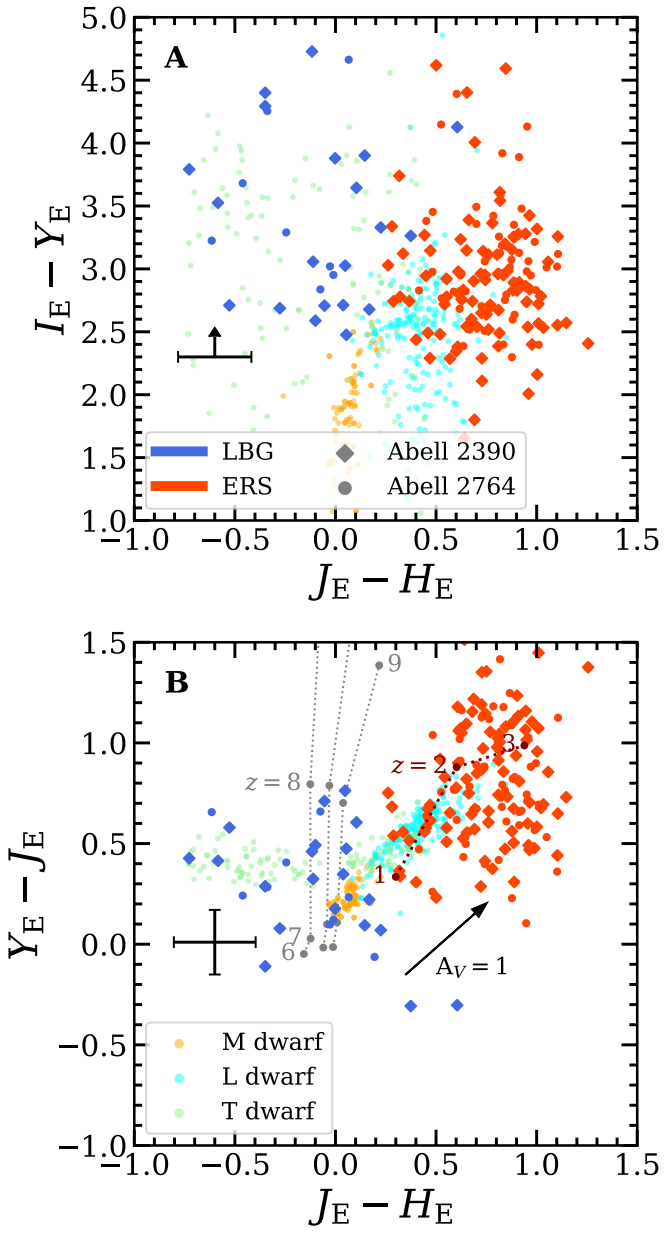

Fig. 2: Selection and properties of 168 NISP-only sources in Abell 2390 and Abell 2764. Sources are divided into Lyman-break galaxy (LBG) candidates and extremely red sources (ERSs). *Panel A*: $I_E - Y_E$ versus $J_E - H_E$ colour-colour diagram highlighting the significance of the VIS non-detection (1.5σ lower limits) and general colours of the sources. *Panel B*: $Y_E - J_E$ versus $J_E - H_E$ colour-colour diagram separating the two samples. Also shown is a reddening vector as well as tracks of z = 6–9 LBGs with different mean stellar ages (grey) and of z = 1–3 maximally old quiescent galaxies (maroon). Colours of observed M-, L-, and T-type dwarf stars are measured from the SpeX Prism Library (Burgasser et al. 2004). Typical colour uncertainties are shown in the upper two panels, where all $I_E - Y_E$ colors are lower limits.

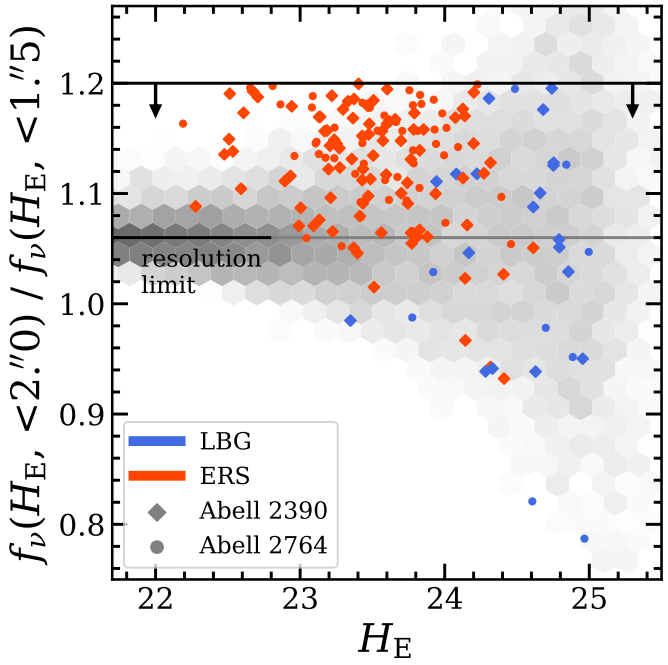

Fig. 3: H_E brightness versus compactness estimated from a flux ratio in 2.″0 to 1.″5 apertures. Selected sources are required to be relatively compact with an aperture ratio below 1.2. The H_E compactness of genuine point sources identified in I_E from the parent catalogue is shown by the grey 2D histogram. Sources below a ratio of 1.0 are visually confirmed to have significantly negative pixels nearby.

4.2. Physical interpretations

To learn more about the possible physical interpretation of these objects, best-fit spectral templates and photometric redshift likelihood distributions, $\mathcal{L}(z)$, were estimated by fitting the photometry using `eazy-py` (Brammer et al. 2008). To avoid contamination from neighbours, total I_E fluxes based on 0.″3 diameter apertures were coupled with total Y_E, J_E, and H_E fluxes based on 1.″2 diameter apertures. At the time of writing, the most comprehensive template set provided with `eazy-py` is `sfhz_blue_agn`, which improves on previous template sets by including a physical prior on allowed star-formation histories to exclude quiescent templates for high-redshift solutions, adding an extreme emission line template suitable for $z > 6$ UV-bright galaxies, and an active galactic nuclei torus template derived from Killi et al. (2023). All priors were turned off, and iterative zero point corrections were not applied.

Having applied `eazy-py`, the differences between the two samples are clarified. While most of the ERSs have bimodal $\mathcal{L}(z)$ distributions, where a $z \approx$ 1–3 quiescent solution is degenerate with a $z \gtrsim 5$ dusty solution, all but two LBG candidates have uniquely best-fit photometric redshift solutions at $z > 6$ and best-fit templates consistent with their classification (the two exceptions are redder in $J_E - H_E$ and have some low-z probability). Figure 4 and 5 show the best-fit template(s), $\mathcal{L}(z)$, and cutouts for two typical examples of ERSs and LBGs, respectively. Also shown are the frame-by-frame lightcurves extracted from each exposure (see Sect.5 for details).

It is difficult to determine the nature of the ERSs conclusively, and it is probably a mixed sample. Contamination from brown dwarfs is likely for unresolved ERSs, given that L-type dwarfs exhibit similar I_E and Y_E, J_E, and H_E colours (Fig. 2). If extragalactic in nature, they could be maximally old quiescent systems at $z \approx$ 1–3 (van Dokkum et al. 2008; Damjanov et al. 2009), or extraordinarily dust-obscured star-forming galaxies at $z \gtrsim 3$ with high stellar masses (e.g., Manning et al. 2022; McKinney et al. 2023; Weaver et al. 2023a). Figure 4 highlights this uncertainty. In principle, deep, high-resolution far-infrared data could distinguish these possibilities, though this first-look study is solely focused on *Euclid* and leaves further investiga-

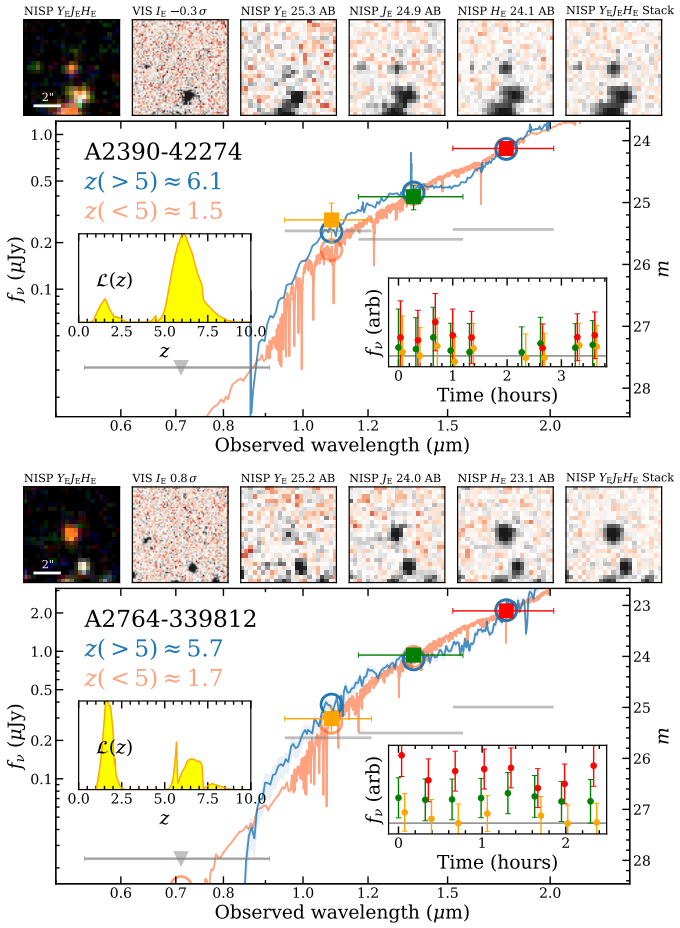

Fig. 4: Two extremely red sources showing their photometry, best-fit templates and bimodal $\mathcal{L}(z)$ from `eazy-py`, cutouts, and light curves. The false colour image is composed from Y_E, J_E, and H_E and the cutouts are scaled linearly such that they saturate at $\pm 3\,\sigma$. Upper limits for I_E are shown by the leftmost grey bar with an arrow, while selection limits for NISP bands are shown as grey bars.

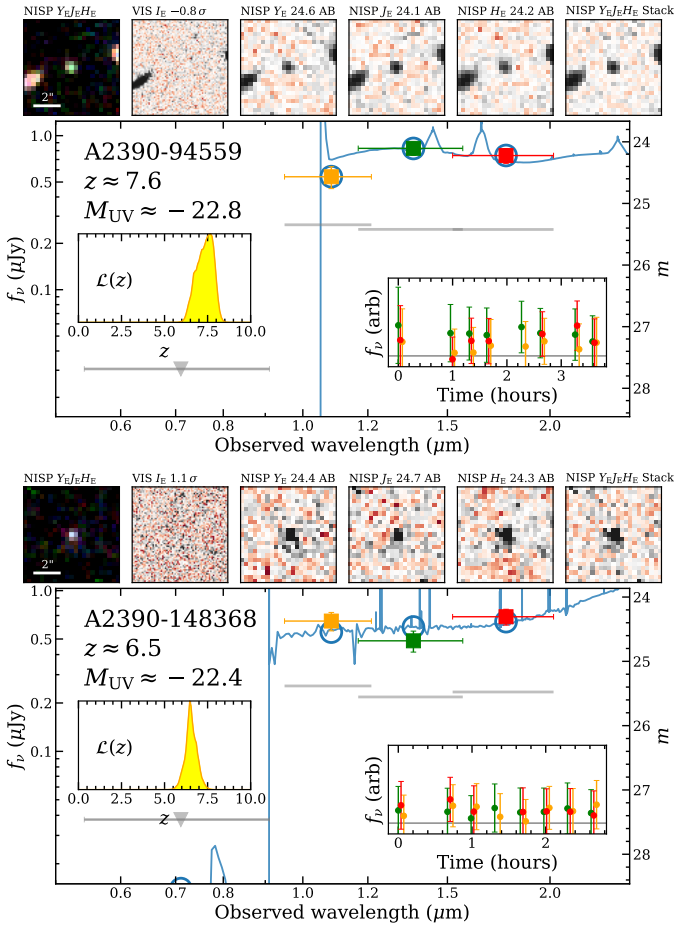

Fig. 5: Two bright Lyman-break galaxy candidates: their photometry, best-fit templates and uniquely high-z $\mathcal{L}(z)$ from `eazy-py`, cutouts, and lightcurves. The false colour image is composed of Y_E, J_E, and H_E and the cutouts are scaled linearly such that they saturate at $\pm 3\,\sigma$. Upper limits for I_E are shown by the leftmost grey bar with an arrow, while selection limits for NISP bands are shown by the grey bars.

tion of these sources for future work. This being said, a cursory inspection of ancillary *Spitzer*/IRAC imaging of the center of Abell 2390[1] detects every one of the six ERS targets they contain, confirming their extremely red nature.

The remaining LBG candidates, taken at face value, are extraordinarily bright objects for such an early epoch. Their rest-frame UV absolute magnitudes M_{UV} from `eazy-py` range from −21.9 to −23.6, comparable to similarly selected samples from UltraVISTA and VIDEO (Bowler et al. 2017; Kauffmann et al. 2022; Varadaraj et al. 2023). If genuine, these rapidly forming systems may be the progenitors of the most massive systems to evolve at later epochs of cosmic history. In addition, they should be valuable tracers of the overdensities in the cosmic web (White & Frenk 1991). Note that while the Abell clusters provide a magnification boost, most LBGs are found far from the cluster core and have magnification factors on the order of unity. Properly delensing the photometry and M_{UV} estimates requires a new lensing model that is not yet in hand.

Although an explicit calculation of the UV luminosity function is beyond the scope of this first-look study, the number densities of the 13 LBGs of $-23 < M_{UV} \leq -22$ at $6.5 < z \leq 7.5$ are comparable to literature estimates of the $z \sim 7$ UV luminosity function of LBGs (~ 10 over 1.5 deg^2, e.g., Bowler et al. 2014; Finkelstein et al. 2015) or of quasars (Schindler et al. 2023; Matsuoka et al. 2023). This is encouraging given the uncertainties associated with photometry, redshifts, possible source magnification, and potential interlopers.

5. Discussion

Given that the EROs are only a first look at the *Euclid* mission, the primary goal of this work is simply to present a sample of NISP-only sources, describe the challenges encountered, and discuss possible solutions to overcome them. As such, this work refrains from generalising this sample to population statistics (e.g. the UV luminosity function), leaving such investigation to near-future *Euclid* studies where the 53 deg^2 of Euclid Deep Survey and Auxillary Fields can be leveraged.

5.1. The expected appearance of high-z sources

Although VIS, with its finely sampled PSF, operates at the diffraction-limited resolution afforded by *Euclid* outside the Earth's atmosphere, the broader PSF of NISP is still undersam-

[1] Confirming these sources is difficult because HST coverage of Abell 2390 is limited to the very core where no LBG or ERO source is found. Further, no ancillary HST or *Spitzer* data exist for Abell 2764.

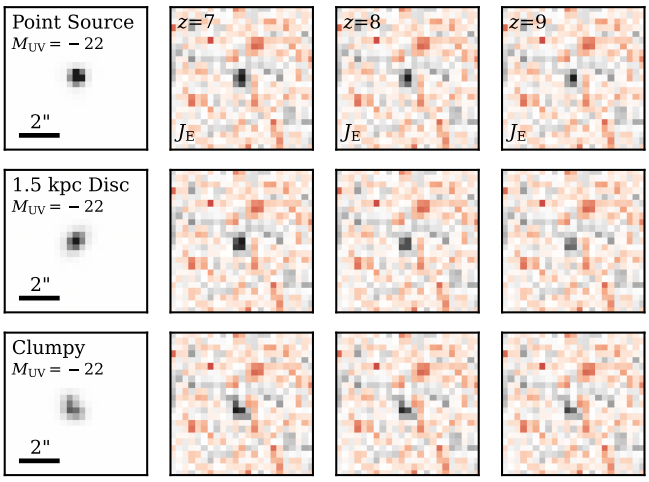

Fig. 6: Models of a $M_{UV} \approx -22$ AB galaxy at z = 7, 8, and 9 assuming three different morphologies: a point source; a 1.5 kpc disc; and a three-point-source clump of similar effective size simulated with `The Tractor` (Lang et al. 2016) and injected into a small empty region of the J_E mosaic at native 0.″3 pix^{-1} scale.

pled at a native 0.″3 pix^{-1} resolution, although "drizzling" can improve this. This effect is highly relevant for assessing morphologies of high-redshift galaxy candidates, since traditional techniques developed from e.g., HST, typically use compactness to separate real point-sources (e.g. stars) from marginally resolved compact galaxies. This technique cannot be applied to sources only found in NISP, where the superior resolution of VIS cannot be leveraged. Figure 6 demonstrates this effect by injecting an $M_{UV} = -22$ source into an empty region of the H_E image of Abell 2390 (with the same result in Abell 2764) with three light distributions: a point source; a 1.5 kpc disc; and a tight clump of three point sources with a similar overall effective size of bright multi-component $z \approx 7$ LBGs found by Bowler et al. (2017). The observed morphology in NISP at 0.″3 pix^{-1} scale in the ERO data is virtually the same for all three cases, and by $z \approx 9$ is indistinguishable given the low S/N. As such, no attempt was made to separate candidates from stars based on their observed morphologies, although this may be possible in the future by combining the frames on a higher-resolution grid (e.g. with "drizzling").

5.2. The probability of brown dwarf contaminants

It is well known that searches for genuine high-redshift LBGs are complicated by late-type MLT dwarf stars because they have similar NIR colours and little optical flux (Bowler et al. 2012, 2014; Varadaraj et al. 2023; Harikane et al. 2022). To illustrate this overlap, I_E, Y_E, J_E, and H_E based colours were measured from observed spectra of M-, L-, and T-type dwarfs compiled in the SpeX prism spectral library of Burgasser et al. (2004) and are shown alongside the sample in Fig. 2 by orange, cyan, and green points, respectively. While the Y_E, J_E, H_E colour-colour space shows that this sample is degenerate with M-, L-, and T-type dwarfs, the requirement of S/N < 1.5 in I_E and $Y_E \gtrsim 25.5$ demands that candidates have an extraordinarily strong break with $I_E - Y_E > 2$. Furthermore, such a strong optical-NIR break is only expected from L- and T-type dwarfs, implying that the depth of I_E relative to that of Y_E effectively excludes M-types by virtue of the ROS design. Furthermore, the factor of 2 discrepancy between the two fields is consistent with the expected (but highly uncertain) sky density of T-type dwarfs as illustrated in Fig. 7, suggesting that from a statistical standpoint that there may be a non-negligible population of T-type dwarf interlopers (see Wood et al., in prep.). In absence of suitably deep ancillary data, a definitive characterisation of these ERO sources requires follow-up spectroscopy and will have to wait for future work.

5.3. Identifying cases of persistence

The *Euclid* mission follows a consistent survey pattern wherein a single visit consists of four dithered pointings with simultaneous observing by VIS and NISP enabled by splitting the primary beam with a dichroic filter (see Euclid Collaboration: Scaramella et al. 2022 for details). While VIS integrates for an ultra-deep image ($I_E \approx 26$ per ROS), NISP begins with a 574-s integration of one of the two grism filters followed in order by equal 112-s integrations of J_E, H_E, and then Y_E ($Y_E, J_E, H_E \approx 25.4$ per ROS). The order is important, since the NIR detectors of NISP are susceptible to charge persistence. This is where some charge from a previous exposure is trapped within the lattice defects of the NISP pixels. This manifests as a faint imprint of the previous exposures (grism or photometry) taken as much as 6-hours earlier.

The persistence signal within the EROs was modelled and subtracted from each ERO exposure. The persistence model was based on the flux of unsaturated pixels within all exposures taken up to 1 hour before the ERO exposure; see Sect. 4.3.1 of Cuillandre et al. (2024) for details. However, strong persistence (>70 ADU) was not modelled because it would leave visible residuals. Therefore, we checked whether this left-over persistence impacted our detection of ERSs and LBGs.

Most of the brightest identifiable spectral persistence was successfully identified, modelled, and subtracted following the procedure developed specifically for the handling of the EROs. Furthermore, since the morphology of the persistence introduced

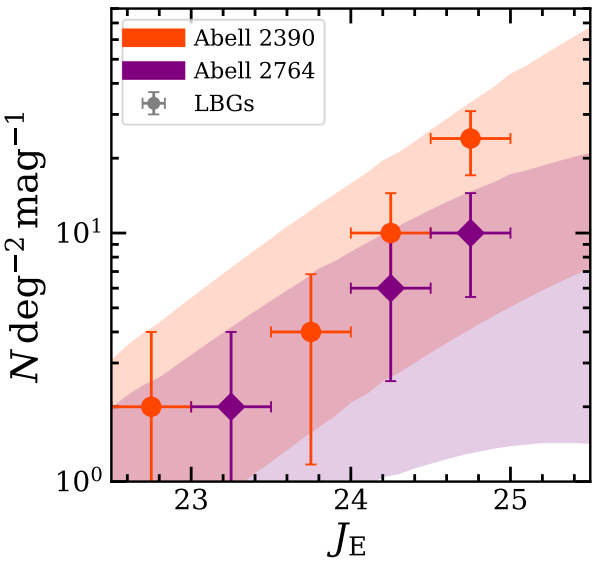

Fig. 7: The number density of selected LBG candidates in Abell 2390 (orange diamonds) and Abell 2764 (purple diamons) compared to a range of T-type dwarf stars (700–1300 K) number densities at the Galactic latitudes of each field. Dwarf sky densities are highly uncertain and are estimated assuming a Solar position of 27 pc above the Galactic plane, an exponential radial scale height of 2250 pc with a vertical scale length of 300 pc (Ryan et al. 2022). See Wood et al., in prep. for details.

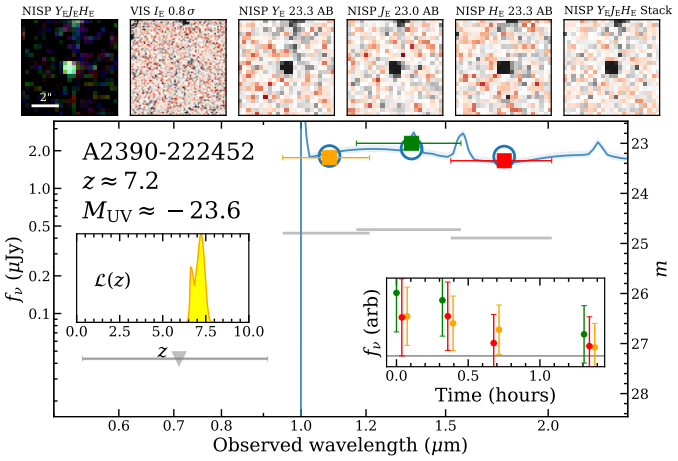

Fig. 8: Example of a bright quasar-like object seen only in Y_E, J_E, and H_E. Time-series analysis of its frame-by-frame photometry reveals a decaying signal suggestive of persistence.

by a stimulus from grism observations follows that of the original spectral trace of the object, the compactness criteria outlined in Sect. 3 effectively rejects the largest of remaining artefacts. However, there are some possible situations in which persistence may remain in the exposures and impact the detection of ERSs and LBGs. One such situation is persistence from cosmic rays in the same ROS sequence (which originally saturated the detector). Another persistence source is saturated compact sources from observations of a previous ROS. Since the persistence signal, P, is expected to decay approximately like $P_{J_E} \approx f_\nu/200$, $P_{H_E} \approx P_{J_E}/2$, and $P_{Y_E} \approx P_{J_E}/3$ for a typical exposure, the spectral colours $J_E < H_E < Y_E$ expected of persistence can mimic a $z \gtrsim 6$ galaxy with appreciable Lyα emission or an extremely steep UV slope.

To facilitate the identification of such artefacts, light curves are constructed for each source by measuring their photometry in each pointing from all 12 exposures. Cosmic ray rejection and persistence cleaning are applied self-consistently to the mosaics and per-detector backgrounds are subtracted as 3σ-clipped medians. Lacking calibrated weight maps, on-the-fly photometric uncertainties are estimated by the standard deviation of the fluxes from 10 000 empty apertures placed around each image.

An example of suspected persistence is shown in Fig. 8. If genuine, the stimulus occurred before or at the start of the observations of Abell 2390, unlike the spectro-to-photo persistence case mentioned above. However, while lightcurves are useful to rule out persistence in the case of bright sources, faint objects that are undetected in individual exposures ($Y_E, J_E, H_E \approx 24$) will remain unidentifiable from a time series analysis. Given the expected exponential form of the UV luminosity function, the most common class of LBGs will be sufficiently faint to avoid detection in individual frames. While there were more obvious cases of persistence in earlier reductions that necessitated this lightcurve analysis, the removal of persistence in the ERO data improved significantly and the number of suspected cases diminished. In the final reductions we found no more extreme case than the candidate showed in Fig 8, and so without absolute certainly declined to remove other candidates. Thankfully, the existence of complementary data from multiple optical and infrared facilities will greatly improve the prospects for identifying NISP-only artefacts (see the section below for details).

5.4. Outlook for Euclid Deep Fields

Upon their completion, the Euclid Deep Fields (EDFs) will survey 53 deg^2 across three fields; EDF-North, EDF-South, and EDF-Fornax, at 2 magnitudes deeper than the EWS (Euclid Collaboration: Scaramella et al. 2022), with these two Abell ERO fields of intermediate depth. The 53-fold increase in area and greater depth translates to more than 10 000 LBGs at $z > 7$ and up to 1000 at $z > 8.5$ (see Bowler et al. 2017), providing the first statistically meaningful samples of rare, UV-luminous galaxies in the reionisation era. Such samples will finally enable constraints to be placed on the evolution of the bright-end of the UV luminosity function, among other investigations. The lessons learned from this work can be applied to the EDFs, since the visit pattern, pointings, and filter order are the same. The only difference is the greater number of visits (i.e., depth), along with more dither positions and position angles which, will improve persistence identification. The methodology laid out in this work is only the start, and will be refined as more data are taken over the survey lifetime.

Two fields in particular, EDF-North and EDF-Fornax, enjoy significant ancillary observations in the UV, optical, and infrared with contributions from both the Hawaii Two-0 Survey and Spitzer Legacy Survey (Euclid Collaboration: Moneti et al. 2022), forming, in conjunction with *Euclid*, a part of the Cosmic Dawn Survey (DAWN). The availability of deep optical data from CFHT Megacam/U and Subaru HSC/$grizy$ will improve the robustness of the candidates found, reveal more about their physical properties, and extend drop-out searches to lower redshifts. Observed over 6000 hours, the Spitzer Legacy Survey provides deep 3.6- and 4.5-μm IRAC imaging necessary to constrain the young stellar populations of $z \gtrsim 3$ galaxies, when H_E becomes a rest-UV indicator. Furthermore, detection of NISP-only sources by IRAC rules out artefacts such as persistence and gives a lever-arm to better identify contaminating brown dwarfs, thereby greatly improving the purity of future LBG and ERS samples (Euclid Collaboration: van Mierlo et al. 2022).

Zalesky et al. (in prep.) has established pre-*Euclid* optically-selected photometric redshift catalogues in EDF-North and EDF-Fornax. While apertures used in the present work are highly effective, obtaining robust photometry of IRAC sources at their characteristically low resolution benefits significantly from fitting galaxy light profiles, e.g. with `The Farmer` (Weaver et al. 2023b). With the addition of I_E, Y_E, J_E, and H_E data, DAWN will provide NIR-selected catalogues of some 20 million sources across EDF-North and EDF-Fornax with robust photometric redshifts and galaxy stellar masses out to $z \approx 10$. Additional complementary data from ongoing spectroscopic campaigns from Keck/DEIMOS and Keck/MOSFIRE, together with the invaluable NISP grism observations, will provide excellent calibration of photometric redshifts and derived physical properties. The unprecedented statistical power achieved by combining *Euclid*, CFHT, Subaru, and *Spitzer* will establish EDF-North and EDF-Fornax as the leading extragalactic fields visible from the northern hemisphere for the next decade. Rich volume-complete samples of LBGs at $z = 6$–10 will provide definitive constraints on the number density and evolution of UV-luminous galaxies necessary to firmly challenge and ultimately refine theories of galaxy formation.

6. Summary

This paper presents one of the first science results from *Euclid*, leveraging the deep degree-scale NIR imaging with NISP

to identify rare, UV-bright LBGs and extremely red sources that are not seen in smaller blank fields. Our larger aim to obtain large samples to provide the statistical power from which their abundance, redshifts, and physical properties can be definitively studied.

Over half a million sources are detected from the twin 0.75 deg^2 Y_E, J_E, and H_E images, and their I_E, Y_E, J_E, and H_E photometry is extracted from apertures corrected to total flux. Photometric redshifts and best-fit galaxy templates are estimated from `eazy-py`. The result is a highly bimodal sample spanning a range of spectral colours, with the following two classes of object.

- 29 sources have flat f_ν colours indicative of $z \approx 6$–8 Lyman break galaxies. Without magnification estimates, their M_{UV} spans −21.9 to −23.6, making this one of the largest samples of UV-luminous high-redshift galaxy candidates found thus far. Contamination by quasars and T-type dwarfs is likely and still needs to be determined.
- 139 sources have extremely red colors indicative of either $z \gtrsim 5$ dusty star-forming galaxies or $z \approx 1$–3 quiescent galaxies. Their redshift distributions are multi-modal, suggesting a mixture. A minority are point-like, which may be contamination by L-type dwarfs.

By selection, these objects are relatively compact, as anticipated for high-redshift LBGs. However, the morphological complexity of real LBGs seen with HST is less distinguishable here due to the $0\farcs3\,\mathrm{pix}^{-1}$ scale of NISP. As a result, artefacts, such as instrumental persistence, cannot be identified from their morphologies. Instead, this work explores the novel use of time series analysis to identify characteristics unique to persistence from the lightcurves of suspected sources. This will be applicable to future *Euclid* observations.

These comparably large samples of NISP-only sources will be dwarfed by those found imminently from the Euclid Deep Fields. EDF-North and EDF-Fornax, in particular, have deep optical Subaru/HSC and *Spitzer*/IRAC coverage, which not only provides a longer lever-arm to identify brown dwarfs, but also a means to immediately identify artefacts arising only in NISP. Upon its completion, the Subaru-*Euclid*-*Spitzer* Cosmic Dawn Survey will identify thousands of similarly UV-luminous galaxies at $z > 6$. These and other future searches will build on lessons learned from this work – the first foray into the distant Universe with *Euclid*.

Acknowledgements. The Cosmic Dawn Center (DAWN) is funded by the Danish National Research Foundation (DNRF140). HA is supported by the French Centre National d'Etudes Spatial (CNES). This work has made use of the `CANDIDE` Cluster at the *Institut d'Astrophysique de Paris* (IAP), made possible by grants from the PNCG and the region of Île de France through the program DIM-ACAV+, and the Cosmic Dawn Center and maintained by S. Rouberol. CS acknowledges the support of the NSERC Postdoctoral Fellowship and the CITA National Fellowship programs. This research has benefited from the SpeX Prism Spectral Libraries, maintained by Adam Burgasser at `http://www.browndwarfs.org/spexprism`. This work made use of Astropy (`http://www.astropy.org`): a community-developed core Python package and an ecosystem of tools and resources for astronomy (Astropy Collaboration et al. 2013, 2018, 2022) and Matplotlib (Hunter 2007). This work has made use of the Early Release Observations (ERO) data from the *Euclid* mission of the European Space Agency (ESA), 2024, `https://doi.org/10.57780/esa-qmocze3`. The Euclid Consortium acknowledges the European Space Agency and a number of agencies and institutes that have supported the development of *Euclid*, in particular the Agenzia Spaziale Italiana, the Austrian Forschungsförderungsgesellschaft, funded through BMK, the Belgian Science Policy, the Canadian Euclid Consortium, the Deutsches Zentrum für Luft- und Raumfahrt, the DTU Space and the Niels Bohr Institute in Denmark, the French Centre National d'Etudes Spatiales, the Fundação para a Ciência e a Tecnologia, the Hungarian Academy of Sciences, the Ministerio de Ciencia, Innovación y Universidades, the National Aeronautics and Space Administration, the National Astronomical Observatory of Japan, the Netherlandse Onderzoekschool Voor Astronomie, the Norwegian Space Agency, the Research Council of Finland, the Romanian Space Agency, the State Secretariat for Education, Research, and Innovation (SERI) at the Swiss Space Office (SSO), and the United Kingdom Space Agency. A complete and detailed list is available on the *Euclid* web site (`http://www.euclid-ec.org`).

References

Adams, N. J., Conselice, C. J., Austin, D., et al. 2024, ApJ, 965, 169
Algera, H. S. B., Inami, H., Sommovigo, L., et al. 2024, MNRAS, 527, 6867
Astropy Collaboration, Price-Whelan, A. M., Lim, P. L., et al. 2022, ApJ, 935, 167
Astropy Collaboration, Price-Whelan, A. M., Sipőcz, B. M., et al. 2018, AJ, 156, 123
Astropy Collaboration, Robitaille, T. P., Tollerud, E. J., et al. 2013, A&A, 558, A33
Atek, H., Gavazzi, R., Weaver, J., et al. 2024a, A&A, this issue
Atek, H., Labbé, I., Furtak, L. J., et al. 2024b, Nature, 626, 975
Bañados, E., Venemans, B. P., Mazzucchelli, C., et al. 2018, Nature, 553, 473
Barbary, K. 2016, Journal of Open Source Software
Barrufet, L., Oesch, P., Marques-Chaves, R., et al. 2024, arXiv e-prints, arXiv:2404.08052
Behroozi, P., Wechsler, R. H., Hearin, A. P., & Conroy, C. 2019, MNRAS, 488, 3143
Bertin, E. & Arnouts, S. 1996, A&AS, 117, 393
Bertin, E., Mellier, Y., Radovich, M., et al. 2002, in Astronomical Society of the Pacific Conference Series, Vol. 281, Astronomical Data Analysis Software and Systems XI, ed. D. A. Bohlender, D. Durand, & T. H. Handley, 228
Bouwens, R., Illingworth, G., Oesch, P., et al. 2023, MNRAS, 523, 1009
Bouwens, R. J., Illingworth, G. D., Oesch, P. A., et al. 2015, ApJ, 811, 140
Bowler, R. A. A., Dunlop, J. S., McLure, R. J., et al. 2012, MNRAS, 426, 2772
Bowler, R. A. A., Dunlop, J. S., McLure, R. J., & McLeod, D. J. 2017, MNRAS, 466, 3612
Bowler, R. A. A., Dunlop, J. S., McLure, R. J., et al. 2014, MNRAS, 440, 2810
Bowler, R. A. A., Inami, H., Sommovigo, L., et al. 2024, MNRAS, 527, 5808
Bowler, R. A. A., Jarvis, M. J., Dunlop, J. S., et al. 2020, MNRAS, 493, 2059
Brammer, G. B., van Dokkum, P. G., & Coppi, P. 2008, ApJ, 686, 1503
Burgasser, A. J., McElwain, M. W., Kirkpatrick, J. D., et al. 2004, AJ, 127, 2856
Carnall, A. C., McLure, R. J., Dunlop, J. S., et al. 2023, Nature, 619, 716
Chemerynska, I., Atek, H., Furtak, L. J., et al. 2023, arXiv e-prints, arXiv:2312.05030
Conroy, C. & Gunn, J. E. 2010, ApJ, 712, 833
Conroy, C., Gunn, J. E., & White, M. 2009, ApJ, 699, 486
Cuillandre, J.-C., Bertin, E., Molzonella, M., et al. 2024, A&A, this issue
Damjanov, I., McCarthy, P. J., Abraham, R. G., et al. 2009, ApJ, 695, 101
Dayal, P. & Ferrara, A. 2018, Phys. Rep., 780, 1
Dayal, P., Volonteri, M., Greene, J. E., et al. 2024, arXiv e-prints, arXiv:2401.11242
Donnan, C. T., McLeod, D. J., Dunlop, J. S., et al. 2023, MNRAS, 518, 6011
Donnan, C. T., McLure, R. J., Dunlop, J. S., et al. 2024, arXiv e-prints, arXiv:2403.03171
Duncan, K., Conselice, C. J., Mortlock, A., et al. 2014, MNRAS, 444, 2960
Endsley, R., Stark, D. P., Bouwens, R. J., et al. 2022, MNRAS, 517, 5642
Endsley, R., Stark, D. P., Whitler, L., et al. 2023, MNRAS, 524, 2312
Euclid Collaboration: Cropper, M., Al Bahlawan, A., Amiaux, J., et al. 2024, A&A, this issue
Euclid Collaboration: Jahnke, K., Gillard, W., Schirmer, M., et al. 2024, A&A, this issue
Euclid Collaboration: Mellier, Y., Acevedo Barroso, J., & Achúcarro, A. o. 2024, A&A, this issue
Euclid Collaboration: Moneti, A., McCracken, H. J., Shuntov, M., et al. 2022, A&A, 658, A126
Euclid Collaboration: Scaramella, R., Amiaux, J., Mellier, Y., et al. 2022, A&A, 662, A112
Euclid Collaboration: Schirmer, M., Jahnke, K., Seidel, G., et al. 2022, A&A, 662, A92
Euclid Collaboration: van Mierlo, S. E., Caputi, K. I., Ashby, M., et al. 2022, A&A, 666, A200
Euclid Collaboration: Zalesky, L. et al. 2024, A&A
Euclid Early Release Observations. 2024, `https://doi.org/10.57780/esa-qmocze3`
Finkelstein, S. L., D'Aloisio, A., Paardekooper, J.-P., et al. 2019, ApJ, 879, 36
Finkelstein, S. L., Ryan, Russell E., J., Papovich, C., et al. 2015, ApJ, 810, 71
Fitzpatrick, E. L. & Massa, D. 2007, ApJ, 663, 320
Franco, M., Elbaz, D., Béthermin, M., et al. 2018, A&A, 620, A152
Furtak, L. J., Labbé, I., Zitrin, A., et al. 2023, arXiv e-prints, arXiv:2308.05735

Glazebrook, K., Nanayakkara, T., Schreiber, C., et al. 2023, arXiv e-prints, arXiv:2308.05606
Gottumukkala, R., Barrufet, L., Oesch, P. A., et al. 2024, MNRAS, 530, 966
Greene, J. E., Labbe, I., Goulding, A. D., et al. 2024, ApJ, 964, 39
Harikane, Y., Ono, Y., Ouchi, M., et al. 2022, ApJS, 259, 20
Harikane, Y., Ouchi, M., Oguri, M., et al. 2023, ApJS, 265, 5
Hunter, J. D. 2007, Computing in Science and Engineering, 9, 90
Jarvis, M. J., Bonfield, D. G., Bruce, V. A., et al. 2013, MNRAS, 428, 1281
Johnson, B., Foreman-Mackey, D., Sick, J., et al. 2023, dfm/python-fsps: v0.4.6
Juodžbalis, I., Conselice, C. J., Singh, M., et al. 2023, MNRAS, 525, 1353
Katgert, P., Mazure, A., Perea, J., et al. 1996, A&A, 310, 8
Kauffmann, O. B., Ilbert, O., Weaver, J. R., et al. 2022, A&A, 667, A65
Killi, M., Watson, D., Brammer, G., et al. 2023, arXiv e-prints, arXiv:2312.03065
Koekemoer, A. M., Faber, S. M., Ferguson, H. C., et al. 2011, ApJS, 197, 36
Kokorev, V., Fujimoto, S., Labbe, I., et al. 2023, ApJ, 957, L7
Lang, D., Hogg, D. W., & Mykytyn, D. 2016, The Tractor: Probabilistic astronomical source detection and measurement, Astrophysics Source Code Library, record ascl:1604.008
Laureijs, R., Amiaux, J., Arduini, S., et al. 2011, arXiv:1110.3193
Leung, G. C. K., Bagley, M. B., Finkelstein, S. L., et al. 2023, ApJ, 954, L46
Lu, T.-Y., Mason, C. A., Hutter, A., et al. 2024, MNRAS, 528, 4872
Manning, S. M., Casey, C. M., Zavala, J. A., et al. 2022, ApJ, 925, 23
Matsuoka, Y., Onoue, M., Iwasawa, K., et al. 2023, ApJ, 949, L42
McCracken, H. J., Milvang-Jensen, B., Dunlop, J., et al. 2012, A&A, 544, A156
McKinney, J., Manning, S. M., Cooper, O. R., et al. 2023, ApJ, 956, 72
Naidu, R. P., Oesch, P. A., Setton, D. J., et al. 2022a, arXiv e-prints, arXiv:2208.02794
Naidu, R. P., Oesch, P. A., van Dokkum, P., et al. 2022b, ApJ, 940, L14
Nelson, E. J., Suess, K. A., Bezanson, R., et al. 2023, ApJ, 948, L18
Neyer, M., Smith, A., Kannan, R., et al. 2023, arXiv e-prints, arXiv:2310.03783
Oke, J. B. 1974, ApJS, 27, 21
Planck Collaboration, Ade, P. A. R., Aghanim, N., et al. 2016, A&A, 594, A13
Qin, Y., Duffy, A. R., Mutch, S. J., et al. 2019, MNRAS, 487, 1946
Roberts-Borsani, G., Treu, T., Chen, W., et al. 2023, Nature, 618, 480
Ryan, R. E., Thorman, P., Aganze, C., et al. 2022, ApJ, 932, 96
Schindler, J.-T., Bañados, E., Connor, T., et al. 2023, ApJ, 943, 67
Schlafly, E. F. & Finkbeiner, D. P. 2011, ApJ, 737, 103
Schouws, S., Bouwens, R., Smit, R., et al. 2023, ApJ, 954, 103
Sohn, J., Fabricant, D. G., Geller, M. J., Hwang, H. S., & Diaferio, A. 2020, ApJ, 902, 17
Trac, H., Cen, R., & Mansfield, P. 2015, ApJ, 813, 54
van Dokkum, P. G., Franx, M., Kriek, M., et al. 2008, ApJ, 677, L5
Varadaraj, R. G., Bowler, R. A. A., Jarvis, M. J., Adams, N. J., & Häußler, B. 2023, MNRAS, 524, 4586
Wang, T., Elbaz, D., Schreiber, C., et al. 2016, ApJ, 816, 84
Wang, T., Schreiber, C., Elbaz, D., et al. 2019, Nature, 572, 211
Wang, T., Sun, H., Zhou, L., et al. 2024, arXiv e-prints, arXiv:2403.02399
Weaver, J. R., Cutler, S. E., Pan, R., et al. 2024, ApJS, 270, 7
Weaver, J. R., Davidzon, I., Toft, S., et al. 2023a, A&A, 677, A184
Weaver, J. R., Zalesky, L., Kokorev, V., et al. 2023b, ApJS, 269, 20
White, S. D. M. & Frenk, C. S. 1991, ApJ, 379, 52
Williams, C. C., Alberts, S., Ji, Z., et al. 2023, arXiv e-prints, arXiv:2311.07483
Zavala, J. A., Buat, V., Casey, C. M., et al. 2023, ApJ, 943, L9
Zavala, J. A., Casey, C. M., Manning, S. M., et al. 2021, ApJ, 909, 165

[1] Department of Astronomy, University of Massachusetts, Amherst, MA 01003, USA
[2] Physics and Astronomy Department, University of California, 900 University Ave., Riverside, CA 92521, USA
[3] Cosmic Dawn Center (DAWN), Denmark
[4] Niels Bohr Institute, University of Copenhagen, Jagtvej 128, 2200 Copenhagen, Denmark
[5] Institute for Astronomy, University of Hawaii, 2680 Woodlawn Drive, Honolulu, HI 96822, USA
[6] Cosmic Dawn Center (DAWN)
[7] Institut d'Astrophysique de Paris, UMR 7095, CNRS, and Sorbonne Université, 98 bis boulevard Arago, 75014 Paris, France
[8] Jodrell Bank Centre for Astrophysics, Department of Physics and Astronomy, University of Manchester, Oxford Road, Manchester M13 9PL, UK
[9] Jet Propulsion Laboratory, California Institute of Technology, 4800 Oak Grove Drive, Pasadena, CA, 91109, USA
[10] Department of Astronomy, School of Science, The University of Tokyo, 7-3-1 Hongo, Bunkyo, Tokyo 113-0033, Japan
[11] Max-Planck-Institut für Astronomie, Königstuhl 17, 69117 Heidelberg, Germany
[12] INAF-Osservatorio di Astrofisica e Scienza dello Spazio di Bologna, Via Piero Gobetti 93/3, 40129 Bologna, Italy
[13] Department of Astronomy, University of Geneva, ch. d'Ecogia 16, 1290 Versoix, Switzerland
[14] School of Physical Sciences, The Open University, Milton Keynes, MK7 6AA, UK
[15] Astrophysics Group, Blackett Laboratory, Imperial College London, London SW7 2AZ, UK
[16] Department of Mathematics, Imperial College London, London SW7 2AZ, UK
[17] School of Physics and Astronomy, University of Nottingham, University Park, Nottingham NG7 2RD, UK
[18] Max Planck Institute for Extraterrestrial Physics, Giessenbachstr. 1, 85748 Garching, Germany
[19] Dipartimento di Fisica e Astronomia "G. Galilei", Università di Padova, Via Marzolo 8, 35131 Padova, Italy
[20] INAF-Osservatorio Astronomico di Padova, Via dell'Osservatorio 5, 35122 Padova, Italy
[21] Instituto de Física de Cantabria, Edificio Juan Jordá, Avenida de los Castros, 39005 Santander, Spain
[22] Aix-Marseille Université, CNRS, CNES, LAM, Marseille, France
[23] Institute for Astronomy, University of Edinburgh, Royal Observatory, Blackford Hill, Edinburgh EH9 3HJ, UK
[24] Institut d'Astrophysique de Paris, 98bis Boulevard Arago, 75014, Paris, France
[25] Université Paris-Saclay, CNRS, Institut d'astrophysique spatiale, 91405, Orsay, France
[26] Observatoire Astronomique de Strasbourg (ObAS), Université de Strasbourg - CNRS, UMR 7550, Strasbourg, France
[27] Kapteyn Astronomical Institute, University of Groningen, PO Box 800, 9700 AV Groningen, The Netherlands
[28] ESAC/ESA, Camino Bajo del Castillo, s/n., Urb. Villafranca del Castillo, 28692 Villanueva de la Cañada, Madrid, Spain
[29] HE Space for European Space Agency (ESA), Camino bajo del Castillo, s/n, Urbanizacion Villafranca del Castillo, Villanueva de la Cañada, 28692 Madrid, Spain
[30] Université Paris-Saclay, Université Paris Cité, CEA, CNRS, AIM, 91191, Gif-sur-Yvette, France
[31] European Space Agency/ESTEC, Keplerlaan 1, 2201 AZ Noordwijk, The Netherlands
[32] Department of Physics, Université de Montréal, 2900 Edouard Montpetit Blvd, Montréal, Québec H3T 1J4, Canada
[33] School of Mathematics and Physics, University of Surrey, Guildford, Surrey, GU2 7XH, UK
[34] INAF-Osservatorio Astronomico di Brera, Via Brera 28, 20122 Milano, Italy
[35] Dipartimento di Fisica e Astronomia, Università di Bologna, Via Gobetti 93/2, 40129 Bologna, Italy
[36] INFN-Sezione di Bologna, Viale Berti Pichat 6/2, 40127 Bologna, Italy
[37] Universitäts-Sternwarte München, Fakultät für Physik, Ludwig-Maximilians-Universität München, Scheinerstrasse 1, 81679 München, Germany
[38] INAF-Osservatorio Astrofisico di Torino, Via Osservatorio 20, 10025 Pino Torinese (TO), Italy
[39] Dipartimento di Fisica, Università di Genova, Via Dodecaneso 33, 16146, Genova, Italy
[40] INFN-Sezione di Genova, Via Dodecaneso 33, 16146, Genova, Italy
[41] Department of Physics "E. Pancini", University Federico II, Via Cinthia 6, 80126, Napoli, Italy
[42] INAF-Osservatorio Astronomico di Capodimonte, Via Moiariello 16, 80131 Napoli, Italy
[43] INFN section of Naples, Via Cinthia 6, 80126, Napoli, Italy
[44] Instituto de Astrofísica e Ciências do Espaço, Universidade do Porto, CAUP, Rua das Estrelas, PT4150-762 Porto, Portugal
[45] Faculdade de Ciências da Universidade do Porto, Rua do Campo de Alegre, 4150-007 Porto, Portugal
[46] Dipartimento di Fisica, Università degli Studi di Torino, Via P. Giuria 1, 10125 Torino, Italy

[47] INFN-Sezione di Torino, Via P. Giuria 1, 10125 Torino, Italy
[48] INAF-IASF Milano, Via Alfonso Corti 12, 20133 Milano, Italy
[49] INAF-Osservatorio Astronomico di Roma, Via Frascati 33, 00078 Monteporzio Catone, Italy
[50] INFN-Sezione di Roma, Piazzale Aldo Moro, 2 - c/o Dipartimento di Fisica, Edificio G. Marconi, 00185 Roma, Italy
[51] Centro de Investigaciones Energéticas, Medioambientales y Tecnológicas (CIEMAT), Avenida Complutense 40, 28040 Madrid, Spain
[52] Port d'Informació Científica, Campus UAB, C. Albareda s/n, 08193 Bellaterra (Barcelona), Spain
[53] Institute for Theoretical Particle Physics and Cosmology (TTK), RWTH Aachen University, 52056 Aachen, Germany
[54] Institute of Space Sciences (ICE, CSIC), Campus UAB, Carrer de Can Magrans, s/n, 08193 Barcelona, Spain
[55] Institut d'Estudis Espacials de Catalunya (IEEC), Edifici RDIT, Campus UPC, 08860 Castelldefels, Barcelona, Spain
[56] Dipartimento di Fisica e Astronomia "Augusto Righi" - Alma Mater Studiorum Università di Bologna, Viale Berti Pichat 6/2, 40127 Bologna, Italy
[57] European Space Agency/ESRIN, Largo Galileo Galilei 1, 00044 Frascati, Roma, Italy
[58] Université Claude Bernard Lyon 1, CNRS/IN2P3, IP2I Lyon, UMR 5822, Villeurbanne, F-69100, France
[59] Institute of Physics, Laboratory of Astrophysics, Ecole Polytechnique Fédérale de Lausanne (EPFL), Observatoire de Sauverny, 1290 Versoix, Switzerland
[60] UCB Lyon 1, CNRS/IN2P3, IUF, IP2I Lyon, 4 rue Enrico Fermi, 69622 Villeurbanne, France
[61] Departamento de Física, Faculdade de Ciências, Universidade de Lisboa, Edifício C8, Campo Grande, PT1749-016 Lisboa, Portugal
[62] Instituto de Astrofísica e Ciências do Espaço, Faculdade de Ciências, Universidade de Lisboa, Campo Grande, 1749-016 Lisboa, Portugal
[63] INAF-Istituto di Astrofisica e Planetologia Spaziali, via del Fosso del Cavaliere, 100, 00100 Roma, Italy
[64] School of Physics, HH Wills Physics Laboratory, University of Bristol, Tyndall Avenue, Bristol, BS8 1TL, UK
[65] INAF-Osservatorio Astronomico di Trieste, Via G. B. Tiepolo 11, 34143 Trieste, Italy
[66] Aix-Marseille Université, CNRS/IN2P3, CPPM, Marseille, France
[67] Istituto Nazionale di Fisica Nucleare, Sezione di Bologna, Via Irnerio 46, 40126 Bologna, Italy
[68] FRACTAL S.L.N.E., calle Tulipán 2, Portal 13 1A, 28231, Las Rozas de Madrid, Spain
[69] Dipartimento di Fisica "Aldo Pontremoli", Università degli Studi di Milano, Via Celoria 16, 20133 Milano, Italy
[70] Institute of Theoretical Astrophysics, University of Oslo, P.O. Box 1029 Blindern, 0315 Oslo, Norway
[71] Leiden Observatory, Leiden University, Einsteinweg 55, 2333 CC Leiden, The Netherlands
[72] Department of Physics, Lancaster University, Lancaster, LA1 4YB, UK
[73] Felix Hormuth Engineering, Goethestr. 17, 69181 Leimen, Germany
[74] Technical University of Denmark, Elektrovej 327, 2800 Kgs. Lyngby, Denmark
[75] NASA Goddard Space Flight Center, Greenbelt, MD 20771, USA
[76] Department of Physics and Helsinki Institute of Physics, Gustaf Hällströmin katu 2, 00014 University of Helsinki, Finland
[77] Mullard Space Science Laboratory, University College London, Holmbury St Mary, Dorking, Surrey RH5 6NT, UK
[78] Université de Genève, Département de Physique Théorique and Centre for Astroparticle Physics, 24 quai Ernest-Ansermet, CH-1211 Genève 4, Switzerland
[79] Department of Physics, P.O. Box 64, 00014 University of Helsinki, Finland
[80] Helsinki Institute of Physics, Gustaf Hällströmin katu 2, University of Helsinki, Helsinki, Finland
[81] Department of Physics and Astronomy, University College London, Gower Street, London WC1E 6BT, UK
[82] NOVA optical infrared instrumentation group at ASTRON, Oude Hoogeveensedijk 4, 7991PD, Dwingeloo, The Netherlands
[83] INFN-Sezione di Milano, Via Celoria 16, 20133 Milano, Italy
[84] Universität Bonn, Argelander-Institut für Astronomie, Auf dem Hügel 71, 53121 Bonn, Germany
[85] Dipartimento di Fisica e Astronomia "Augusto Righi" - Alma Mater Studiorum Università di Bologna, via Piero Gobetti 93/2, 40129 Bologna, Italy
[86] Department of Physics, Centre for Extragalactic Astronomy, Durham University, South Road, DH1 3LE, UK
[87] Infrared Processing and Analysis Center, California Institute of Technology, Pasadena, CA 91125, USA
[88] Université Côte d'Azur, Observatoire de la Côte d'Azur, CNRS, Laboratoire Lagrange, Bd de l'Observatoire, CS 34229, 06304 Nice cedex 4, France
[89] Université Paris Cité, CNRS, Astroparticule et Cosmologie, 75013 Paris, France
[90] University of Applied Sciences and Arts of Northwestern Switzerland, School of Engineering, 5210 Windisch, Switzerland
[91] Institut de Física d'Altes Energies (IFAE), The Barcelona Institute of Science and Technology, Campus UAB, 08193 Bellaterra (Barcelona), Spain
[92] Department of Physics and Astronomy, University of Aarhus, Ny Munkegade 120, DK-8000 Aarhus C, Denmark
[93] Waterloo Centre for Astrophysics, University of Waterloo, Waterloo, Ontario N2L 3G1, Canada
[94] Department of Physics and Astronomy, University of Waterloo, Waterloo, Ontario N2L 3G1, Canada
[95] Perimeter Institute for Theoretical Physics, Waterloo, Ontario N2L 2Y5, Canada
[96] Space Science Data Center, Italian Space Agency, via del Politecnico snc, 00133 Roma, Italy
[97] Centre National d'Etudes Spatiales – Centre spatial de Toulouse, 18 avenue Edouard Belin, 31401 Toulouse Cedex 9, France
[98] Institute of Space Science, Str. Atomistilor, nr. 409 Măgurele, Ilfov, 077125, Romania
[99] INFN-Padova, Via Marzolo 8, 35131 Padova, Italy
[100] Departamento de Física, FCFM, Universidad de Chile, Blanco Encalada 2008, Santiago, Chile
[101] Universität Innsbruck, Institut für Astro- und Teilchenphysik, Technikerstr. 25/8, 6020 Innsbruck, Austria
[102] Satlantis, University Science Park, Sede Bld 48940, Leioa-Bilbao, Spain
[103] Instituto de Astrofísica e Ciências do Espaço, Faculdade de Ciências, Universidade de Lisboa, Tapada da Ajuda, 1349-018 Lisboa, Portugal
[104] Universidad Politécnica de Cartagena, Departamento de Electrónica y Tecnología de Computadoras, Plaza del Hospital 1, 30202 Cartagena, Spain
[105] Institut de Recherche en Astrophysique et Planétologie (IRAP), Université de Toulouse, CNRS, UPS, CNES, 14 Av. Edouard Belin, 31400 Toulouse, France
[106] INFN-Bologna, Via Irnerio 46, 40126 Bologna, Italy
[107] Dipartimento di Fisica, Università degli studi di Genova, and INFN-Sezione di Genova, via Dodecaneso 33, 16146, Genova, Italy
[108] INAF, Istituto di Radioastronomia, Via Piero Gobetti 101, 40129 Bologna, Italy
[109] Institut für Theoretische Physik, University of Heidelberg, Philosophenweg 16, 69120 Heidelberg, Germany
[110] Université St Joseph; Faculty of Sciences, Beirut, Lebanon
[111] Junia, EPA department, 41 Bd Vauban, 59800 Lille, France
[112] IFPU, Institute for Fundamental Physics of the Universe, via Beirut 2, 34151 Trieste, Italy
[113] SISSA, International School for Advanced Studies, Via Bonomea 265, 34136 Trieste TS, Italy
[114] INFN, Sezione di Trieste, Via Valerio 2, 34127 Trieste TS, Italy

[115] ICSC - Centro Nazionale di Ricerca in High Performance Computing, Big Data e Quantum Computing, Via Magnanelli 2, Bologna, Italy
[116] Aurora Technology for European Space Agency (ESA), Camino bajo del Castillo, s/n, Urbanizacion Villafranca del Castillo, Villanueva de la Cañada, 28692 Madrid, Spain
[117] Department of Physics and Astronomy, University of British Columbia, Vancouver, BC V6T 1Z1, Canada

Appendix A: Lyman-break galaxy candidates

This appendix contains Table A.1 describing the coordinates, photometry, photometric redshift, and rest-frame UV magnitudes for the 29 LBG candidates, as well as cutouts in Fig. A.1.

Table A.1: Coordinates, observed photometry, best-fit $z_{\rm phot}$, and corresponding rest-frame UV magnitude ($M_{\rm UV}$) of the Lyman-break galaxy candidates. $I_{\rm E}$ photometry is quoted as 1.5 σ lower limits computed from corrected 0.″6 apertures. $Y_{\rm E}$, $J_{\rm E}$, and $H_{\rm E}$ photometry is quoted as detections from corrected 1.″2 apertures. $M_{\rm UV}$ corresponds to the best-fit $z_{\rm phot}$ taken at the peak of $\mathcal{L}(z)$; these are estimated directly from $J_{\rm E}$, and are uncorrected for lensing magnification.

ID	RA [J2000]	Dec [J2000]	Field	$I_{\rm E}$ [mag]	$Y_{\rm E}$ [mag]	$J_{\rm E}$ [mag]	$H_{\rm E}$ [mag]	$z_{\rm phot}$	$M_{\rm UV}$ [mag]
13405	328.342108	17.264356	A2390	27.45	25.30 ± 0.31	24.86 ± 0.17	25.04 ± 0.19	6.46	−22.14 ± 0.16
19040	328.605616	17.299342	A2390	29.48	24.61 ± 0.27	24.97 ± 0.31	24.44 ± 0.18	6.69	−22.59 ± 0.15
41598	328.143886	17.405425	A2390	27.63	25.51 ± 0.35	25.09 ± 0.19	25.11 ± 0.19	6.46	−22.05 ± 0.17
50473	328.68049	17.44325	A2390	27.90	25.23 ± 0.26	24.96 ± 0.17	25.15 ± 0.19	6.54	−22.03 ± 0.17
58657	328.740945	17.474326	A2390	27.55	24.21 ± 0.09	23.84 ± 0.05	24.64 ± 0.11	6.61	−22.77 ± 0.06
62727	328.129815	17.488942	A2390	27.48	24.39 ± 0.11	24.03 ± 0.07	24.69 ± 0.12	7.17	−22.72 ± 0.08
81797	328.639259	17.552634	A2390	27.48	25.24 ± 0.23	24.71 ± 0.11	25.31 ± 0.19	7.67	−22.19 ± 0.12
93626	328.136037	17.589922	A2390	28.79	25.03 ± 0.18	24.91 ± 0.13	24.99 ± 0.13	7.00	−22.23 ± 0.27
94559	328.711201	17.592819	A2390	30.29	24.80 ± 0.17	24.39 ± 0.09	24.58 ± 0.11	7.67	−22.75 ± 0.16
120148	327.965859	17.674409	A2390	27.24	24.89 ± 0.25	24.86 ± 0.20	25.21 ± 0.26	6.61	−21.98 ± 0.14
148368	327.98274	17.763439	A2390	27.43	24.60 ± 0.13	24.96 ± 0.15	24.66 ± 0.11	6.46	−22.35 ± 0.09
164665	328.719457	17.816599	A2390	28.27	24.88 ± 0.19	24.33 ± 0.10	24.30 ± 0.09	7.17	−22.97 ± 0.08
184757	328.023821	17.885509	A2390	28.84	24.51 ± 0.12	24.67 ± 0.11	25.10 ± 0.16	6.85	−22.21 ± 0.09
191297	328.179802	17.909668	A2390	27.94	25.64 ± 0.32	24.98 ± 0.15	25.11 ± 0.15	7.85	−22.31 ± 0.33
191552	328.470833	17.910763	A2390	28.21	25.18 ± 0.22	25.17 ± 0.18	25.02 ± 0.15	6.61	−22.09 ± 0.12
202358	328.553214	17.953689	A2390	27.67	25.41 ± 0.28	25.11 ± 0.17	25.15 ± 0.17	6.46	−21.97 ± 0.15
212873	328.667034	17.997065	A2390	27.98	25.21 ± 0.31	24.50 ± 0.13	24.52 ± 0.13	7.67	−22.89 ± 0.28
217438	328.28835	18.015891	A2390	27.61	25.37 ± 0.29	25.20 ± 0.20	25.10 ± 0.18	6.32	−21.93 ± 1.07
222452	328.648599	18.037469	A2390	27.40	23.52 ± 0.07	23.28 ± 0.05	23.70 ± 0.07	7.25	−23.60 ± 0.06
239238	328.495839	18.134716	A2390	28.97	25.08 ± 0.21	25.04 ± 0.17	24.97 ± 0.16	6.85	−22.17 ± 0.15
262598	5.804307	−49.705047	A2764	28.10	25.24 ± 0.23	24.63 ± 0.11	25.32 ± 0.20	7.67	−22.24 ± 0.12
268022	5.668767	−49.663003	A2764	27.69	25.18 ± 0.17	25.11 ± 0.13	25.20 ± 0.14	6.39	−21.93 ± 0.23
286717	5.546056	−49.561428	A2764	27.80	25.42 ± 0.23	24.81 ± 0.11	24.96 ± 0.12	7.76	−22.43 ± 0.24
333372	6.024066	−49.390368	A2764	28.35	25.01 ± 0.16	24.82 ± 0.11	25.35 ± 0.18	6.69	−21.95 ± 0.09
351604	5.260838	−49.334863	A2764	30.03	25.01 ± 0.15	24.83 ± 0.11	24.84 ± 0.11	7.00	−22.37 ± 0.11
372941	6.34368	−49.272889	A2764	23.90	24.28 ± 0.08	24.40 ± 0.07	24.28 ± 0.06	6.85	−22.84 ± 0.07
378283	5.768291	−49.25985	A2764	27.92	25.09 ± 0.17	24.73 ± 0.10	25.06 ± 0.14	6.54	−22.16 ± 0.12
455753	5.277561	−49.006585	A2764	27.79	23.95 ± 0.08	23.72 ± 0.05	24.13 ± 0.08	7.25	−23.18 ± 0.07
484507	5.536343	−48.856873	A2764	27.78	25.18 ± 0.25	25.14 ± 0.20	25.24 ± 0.22	6.46	−21.90 ± 0.29

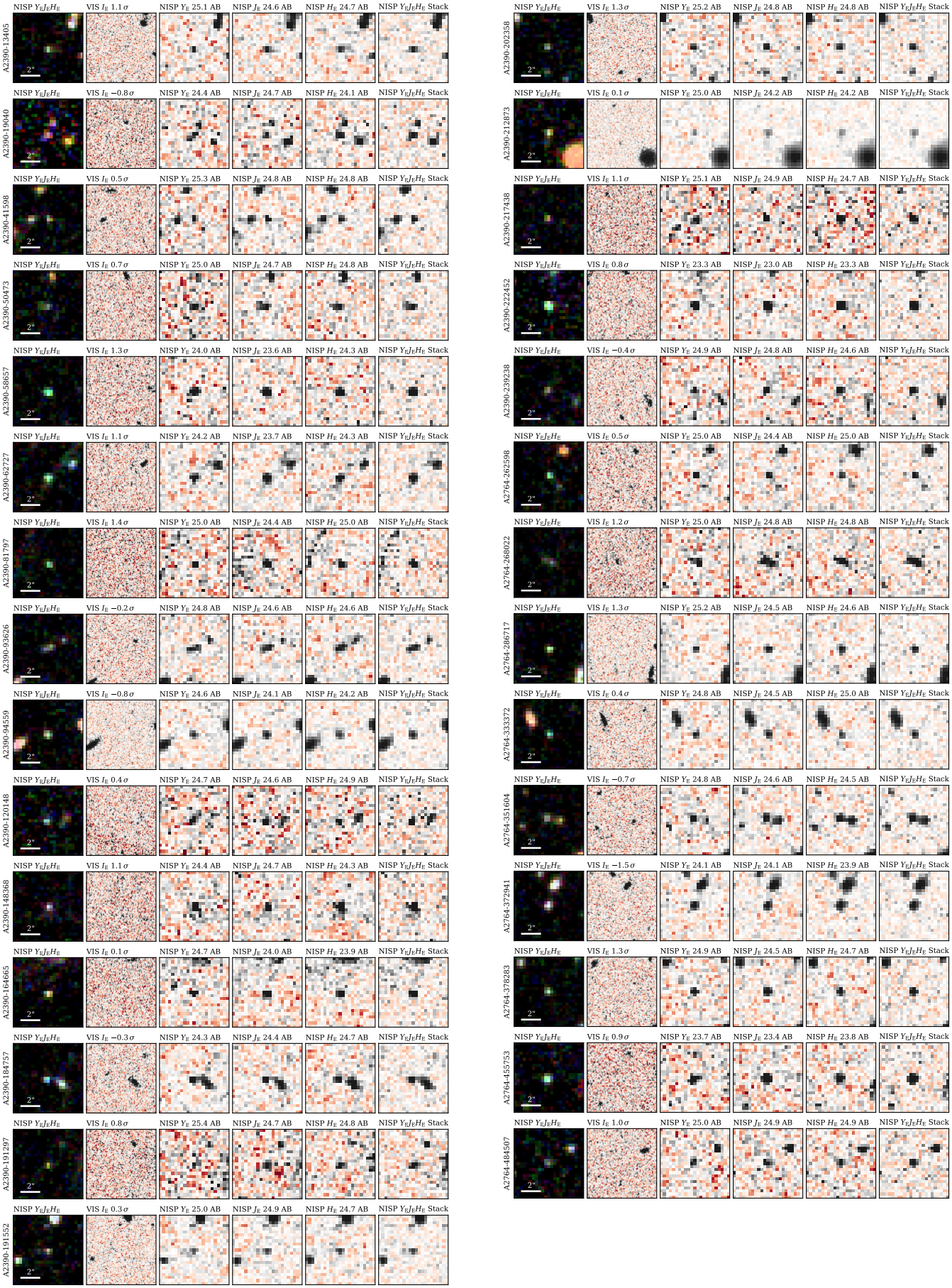

Fig. A.1: Cutouts of $z \approx 6$–8 Lyman break candidates. Leftmost false-colour RBG images are constructed from NISP/Y_E, J_E, H_E. Others show VIS/I_E, NISP/Y_E, J_E, H_E, and the NISP detection stack, scaled to $\pm 3\sigma$ to emphasize the significance of the detections. Cutouts are 5″along a side.

Appendix B: Extremely red sources

This appendix contains Tables B.1, B.2, B.3 and B.4 describing the coordinates, photometry, and photometric redshift solution(s) for the 139 ERSs, as well as cutouts in Figs. B.1, B.2, B.3 and B.4.

Table B.1: Coordinates, observed photometry, best-fit $z_{\rm phot}$, and corresponding redshfit solution(s) of the Extremely Red sources. $I_{\rm E}$ photometry is quoted as 1.5 σ upper limits computed from corrected 0.″6 apertures. $Y_{\rm E}$, $J_{\rm E}$, $H_{\rm E}$ photometry is quoted as detections from corrected 1.″2 apertures. The best-fit photometric redshfit $z_{\rm phot}$ quoted here is taken at the peak of $\mathcal{L}(z > 5)$, with any significant peak at $z < 5$ indicated for bimodal solutions.

ID	RA [J2000]	Dec [J2000]	Field	$I_{\rm E}$ [mag]	$Y_{\rm E}$ [mag]	$J_{\rm E}$ [mag]	$H_{\rm E}$ [mag]	$z_{\rm phot}$	$z_{\rm phot}(< 5)$
1418	328.256848	17.153557	A2390	26.61	24.97 ± 0.32	24.15 ± 0.12	23.50 ± 0.06	5.69	1.44
11725	328.392774	17.251623	A2390	27.22	25.15 ± 0.29	24.51 ± 0.13	23.55 ± 0.05	5.42	1.41
12491	328.192359	17.257306	A2390	27.17	25.14 ± 0.32	24.88 ± 0.21	24.56 ± 0.15	6.32	1.46
17513	328.197604	17.290342	A2390	27.31	25.18 ± 0.25	24.63 ± 0.13	23.75 ± 0.05	5.62	4.99
20071	328.443517	17.304954	A2390	27.38	24.72 ± 0.17	23.79 ± 0.06	23.06 ± 0.03	5.69	1.56
21171	328.51353	17.310914	A2390	27.56	25.00 ± 0.29	24.77 ± 0.19	24.12 ± 0.10	5.89	1.46
29808	328.307984	17.355299	A2390	27.36	25.49 ± 0.29	24.76 ± 0.12	24.24 ± 0.07	5.69	1.46
32789	328.354038	17.369211	A2390	30.90	25.10 ± 0.19	24.92 ± 0.13	24.50 ± 0.08	6.69	–
33926	328.586033	17.373971	A2390	27.92	25.46 ± 0.34	24.46 ± 0.11	23.92 ± 0.07	6.54	1.64
34754	328.338724	17.377432	A2390	27.49	25.00 ± 0.19	24.64 ± 0.11	23.97 ± 0.06	5.82	1.44
42274	328.32914	17.408282	A2390	28.78	25.51 ± 0.30	25.19 ± 0.18	24.48 ± 0.09	6.10	1.51
44724	328.228369	17.418534	A2390	28.27	24.53 ± 0.12	23.92 ± 0.06	23.30 ± 0.03	6.24	–
46207	328.627413	17.425007	A2390	28.06	25.66 ± 0.34	24.56 ± 0.11	23.95 ± 0.06	6.69	1.72
48955	328.365466	17.436572	A2390	28.03	25.15 ± 0.23	24.13 ± 0.07	23.58 ± 0.04	6.54	–
49401	328.311951	17.438465	A2390	27.61	24.78 ± 0.16	23.70 ± 0.05	22.87 ± 0.02	5.69	1.56
52137	328.167879	17.443979	A2390	27.86	25.57 ± 0.31	24.27 ± 0.08	23.59 ± 0.04	7.00	1.83
52813	328.482966	17.45313	A2390	28.00	25.61 ± 0.31	25.15 ± 0.17	24.67 ± 0.10	6.10	1.46
57400	328.673108	17.469908	A2390	27.71	24.88 ± 0.17	24.26 ± 0.08	23.45 ± 0.04	5.89	1.51
61030	328.328541	17.483197	A2390	28.05	25.15 ± 0.22	24.56 ± 0.10	23.53 ± 0.04	5.69	1.39
62830	328.654118	17.489255	A2390	29.31	24.63 ± 0.14	23.60 ± 0.04	22.83 ± 0.02	6.46	–
72934	328.209521	17.524068	A2390	28.32	25.68 ± 0.34	24.59 ± 0.10	23.92 ± 0.05	6.61	1.80
75674	328.335908	17.532969	A2390	27.54	25.72 ± 0.34	24.42 ± 0.09	23.77 ± 0.04	6.92	1.92
86384	328.461045	17.567449	A2390	28.22	25.66 ± 0.36	24.56 ± 0.11	23.69 ± 0.05	5.69	1.61
90220	328.816407	17.579096	A2390	27.67	24.94 ± 0.18	24.02 ± 0.06	23.36 ± 0.03	6.39	1.64
90763	328.4943	17.581134	A2390	27.72	25.50 ± 0.28	24.36 ± 0.08	23.71 ± 0.04	6.69	1.75
90795	328.787715	17.580962	A2390	28.10	25.69 ± 0.33	24.69 ± 0.10	24.14 ± 0.06	6.54	1.64
93645	327.999493	17.589824	A2390	26.57	25.24 ± 0.35	24.72 ± 0.18	24.10 ± 0.10	5.55	1.41
94124	328.048253	17.591283	A2390	27.47	25.45 ± 0.33	24.13 ± 0.08	22.95 ± 0.03	5.69	1.56
94349	328.046741	17.591861	A2390	27.08	24.67 ± 0.16	23.79 ± 0.06	22.97 ± 0.03	5.69	1.51

Table B.2: Continued...

ID	RA [J2000]	Dec [J2000]	Field	I_E [mag]	Y_E [mag]	J_E [mag]	H_E [mag]	z_{phot}	$z_{phot}(< 5)$
96461	328.061955	17.599076	A2390	28.65	25.34 ± 0.27	24.64 ± 0.12	24.05 ± 0.07	6.39	1.56
97193	328.330676	17.601779	A2390	28.04	25.67 ± 0.33	24.71 ± 0.11	23.84 ± 0.05	5.69	1.46
98610	328.026642	17.606334	A2390	27.92	25.19 ± 0.26	24.22 ± 0.09	23.49 ± 0.04	6.32	1.59
99206	328.047244	17.608267	A2390	27.79	25.59 ± 0.35	24.79 ± 0.14	24.17 ± 0.07	6.39	1.56
100728	328.164931	17.613177	A2390	27.91	24.88 ± 0.18	24.47 ± 0.10	23.58 ± 0.04	5.69	–
102521	328.087851	17.618922	A2390	27.34	25.51 ± 0.27	24.88 ± 0.13	24.48 ± 0.09	5.69	1.46
106154	328.294392	17.630897	A2390	27.54	25.05 ± 0.19	24.25 ± 0.07	23.49 ± 0.03	5.69	1.53
110635	328.360005	17.644253	A2390	28.03	25.50 ± 0.30	24.33 ± 0.08	23.72 ± 0.05	6.77	1.77
116975	328.380004	17.664733	A2390	28.23	25.39 ± 0.26	24.83 ± 0.13	24.43 ± 0.08	6.32	–
117303	328.797486	17.665343	A2390	27.61	24.70 ± 0.18	24.07 ± 0.08	23.87 ± 0.06	6.46	–
123765	328.258542	17.685761	A2390	27.87	25.38 ± 0.25	24.63 ± 0.10	23.79 ± 0.05	5.69	1.51
126542	328.00841	17.694133	A2390	27.16	25.46 ± 0.31	24.56 ± 0.12	23.63 ± 0.05	5.69	1.41
126907	328.736884	17.695487	A2390	27.85	25.55 ± 0.32	24.69 ± 0.12	23.96 ± 0.06	5.69	1.53
127591	328.332861	17.697974	A2390	27.70	24.92 ± 0.18	24.50 ± 0.10	23.73 ± 0.05	5.89	–
127981	328.577841	17.699035	A2390	27.52	25.58 ± 0.30	24.53 ± 0.10	23.63 ± 0.04	5.69	1.39
128262	328.131084	17.699773	A2390	27.87	25.10 ± 0.20	24.34 ± 0.08	23.76 ± 0.04	6.39	–
128275	328.649621	17.699791	A2390	27.68	24.96 ± 0.17	24.46 ± 0.09	23.65 ± 0.04	5.82	1.51
130298	327.986255	17.70546	A2390	27.15	25.13 ± 0.26	24.27 ± 0.09	23.82 ± 0.06	5.69	1.61
130523	328.510018	17.706703	A2390	27.65	25.37 ± 0.26	24.60 ± 0.10	24.13 ± 0.06	5.69	1.46
131192	328.655842	17.708628	A2390	23.90	25.63 ± 0.35	25.21 ± 0.20	24.29 ± 0.08	6.10	1.46
132329	328.566782	17.712264	A2390	27.88	25.69 ± 0.32	25.10 ± 0.15	24.50 ± 0.08	5.62	1.48
132673	328.066394	17.71305	A2390	27.59	25.50 ± 0.28	24.90 ± 0.13	24.21 ± 0.07	5.55	1.48
132838	327.951613	17.713357	A2390	28.04	25.21 ± 0.30	24.37 ± 0.11	23.83 ± 0.07	6.54	1.56
134238	328.710895	17.71771	A2390	27.89	25.32 ± 0.23	24.64 ± 0.10	23.86 ± 0.05	5.96	1.51
134239	328.627428	17.71786	A2390	27.47	25.65 ± 0.32	25.05 ± 0.15	24.56 ± 0.09	5.69	1.46
134611	327.928143	17.718602	A2390	26.51	25.28 ± 0.35	23.82 ± 0.08	23.25 ± 0.04	7.17	2.06
135122	328.587476	17.720894	A2390	27.71	25.63 ± 0.35	25.01 ± 0.16	24.63 ± 0.11	5.69	1.46
135949	327.958728	17.723145	A2390	27.07	24.96 ± 0.21	23.57 ± 0.05	22.63 ± 0.02	5.69	1.75
136075	328.570979	17.724072	A2390	27.57	24.75 ± 0.14	23.74 ± 0.05	22.87 ± 0.02	5.69	1.46
139572	327.976023	17.734667	A2390	27.00	25.47 ± 0.32	25.03 ± 0.17	24.14 ± 0.07	5.05	4.99
140449	328.108724	17.737865	A2390	27.68	25.30 ± 0.25	25.01 ± 0.16	24.77 ± 0.12	6.39	–
140700	328.594794	17.738527	A2390	27.83	24.68 ± 0.14	23.77 ± 0.05	23.03 ± 0.02	6.24	–
142039	328.646716	17.742988	A2390	28.00	25.13 ± 0.19	24.87 ± 0.12	24.06 ± 0.05	5.82	–
146825	328.014082	17.75839	A2390	28.23	25.38 ± 0.25	24.83 ± 0.12	24.15 ± 0.06	6.10	1.51
148129	328.622533	17.762907	A2390	27.50	25.59 ± 0.32	24.46 ± 0.09	23.93 ± 0.05	6.92	1.83
152601	327.947827	17.776723	A2390	27.42	25.26 ± 0.24	24.87 ± 0.14	23.84 ± 0.05	5.69	4.99
156298	328.268199	17.788413	A2390	28.39	25.32 ± 0.27	24.79 ± 0.13	23.86 ± 0.05	5.82	1.44
156920	328.643826	17.791403	A2390	27.83	25.72 ± 0.34	24.67 ± 0.11	24.10 ± 0.06	6.46	1.64
159130	328.576532	17.798692	A2390	28.16	25.69 ± 0.33	24.64 ± 0.11	23.83 ± 0.05	5.69	1.56
160963	328.411422	17.804849	A2390	27.69	25.54 ± 0.30	24.86 ± 0.13	23.79 ± 0.05	5.36	4.99
160990	328.428243	17.804948	A2390	28.04	25.53 ± 0.30	25.06 ± 0.16	24.50 ± 0.09	6.10	1.46
162124	328.003353	17.808232	A2390	27.69	25.37 ± 0.23	24.89 ± 0.13	24.67 ± 0.10	6.03	–
174313	328.114589	17.849632	A2390	27.52	25.61 ± 0.31	24.92 ± 0.13	24.18 ± 0.06	5.69	1.39
176069	328.546806	17.855855	A2390	27.93	25.50 ± 0.28	24.85 ± 0.13	23.96 ± 0.06	5.69	1.44
178357	328.58747	17.863986	A2390	28.36	25.04 ± 0.19	24.09 ± 0.06	23.35 ± 0.03	6.32	–

Table B.3: Continued...

ID	RA [J2000]	Dec [J2000]	Field	I_E [mag]	Y_E [mag]	J_E [mag]	H_E [mag]	z_{phot}	$z_{phot}(< 5)$
179032	328.513208	17.866424	A2390	28.42	25.53 ± 0.33	25.02 ± 0.16	24.76 ± 0.13	7.00	–
181995	328.272992	17.876456	A2390	27.49	25.18 ± 0.22	24.56 ± 0.10	23.61 ± 0.04	5.42	1.36
182016	328.623151	17.875228	A2390	28.01	23.97 ± 0.07	23.47 ± 0.04	22.89 ± 0.02	6.24	–
182511	328.608852	17.878096	A2390	29.33	25.52 ± 0.26	25.21 ± 0.17	24.97 ± 0.12	6.85	–
184713	328.066672	17.884999	A2390	27.73	24.89 ± 0.15	24.38 ± 0.08	24.01 ± 0.05	6.03	–
186655	328.063303	17.892486	A2390	27.81	25.50 ± 0.27	24.48 ± 0.09	23.54 ± 0.04	5.69	1.44
190003	328.452507	17.904887	A2390	27.52	25.26 ± 0.24	24.26 ± 0.08	23.57 ± 0.04	5.69	1.66
190359	328.194595	17.906096	A2390	28.34	25.57 ± 0.29	24.77 ± 0.11	23.79 ± 0.04	5.69	1.39
198968	328.498325	17.939391	A2390	28.03	25.57 ± 0.32	24.39 ± 0.09	23.56 ± 0.04	5.69	1.61
200432	328.612065	17.945323	A2390	27.55	25.52 ± 0.31	24.53 ± 0.10	23.79 ± 0.05	5.69	1.56
200510	328.695125	17.945585	A2390	27.21	24.88 ± 0.25	24.42 ± 0.14	24.12 ± 0.10	5.89	–
201258	328.459279	17.948958	A2390	28.08	25.51 ± 0.32	24.99 ± 0.16	24.51 ± 0.10	6.17	1.46
213211	328.052488	17.998072	A2390	27.01	24.55 ± 0.21	24.10 ± 0.11	23.29 ± 0.05	5.75	1.39
217816	328.675502	18.017266	A2390	27.23	24.61 ± 0.20	23.91 ± 0.09	23.73 ± 0.07	6.46	–
227487	328.314319	18.063201	A2390	27.63	25.08 ± 0.22	24.56 ± 0.11	24.18 ± 0.08	5.96	–
255757	5.69298	−49.77244	A2764	27.26	25.43 ± 0.29	25.25 ± 0.21	24.45 ± 0.10	5.62	4.99
258762	5.761004	−49.740345	A2764	27.63	25.69 ± 0.34	25.05 ± 0.16	24.11 ± 0.07	5.42	1.41
260052	5.737694	−49.727595	A2764	27.93	24.45 ± 0.10	23.85 ± 0.05	23.01 ± 0.02	5.96	–
275980	5.910008	−49.614452	A2764	27.68	25.08 ± 0.18	24.10 ± 0.06	23.22 ± 0.03	5.69	1.46
276361	5.623303	−49.61231	A2764	27.93	25.38 ± 0.21	25.02 ± 0.12	24.28 ± 0.06	5.82	1.44
277056	5.591612	−49.608529	A2764	27.64	25.59 ± 0.28	24.76 ± 0.11	24.09 ± 0.06	5.69	1.53
277236	5.504416	−49.607464	A2764	28.22	25.50 ± 0.29	25.20 ± 0.19	24.17 ± 0.07	5.69	4.99
279750	5.565212	−49.594306	A2764	27.75	25.67 ± 0.27	24.94 ± 0.12	24.35 ± 0.07	5.69	1.51
290229	5.931895	−49.546567	A2764	27.81	25.59 ± 0.27	24.53 ± 0.08	23.84 ± 0.04	5.69	1.69
297920	5.346424	−49.514259	A2764	27.89	25.61 ± 0.32	24.83 ± 0.13	24.02 ± 0.06	5.69	1.51
300371	5.429171	−49.50444	A2764	27.96	25.62 ± 0.27	24.90 ± 0.12	24.14 ± 0.06	5.62	1.51
307317	5.5597	−49.478114	A2764	27.99	25.06 ± 0.17	24.22 ± 0.07	23.60 ± 0.04	6.39	–
311115	6.063442	−49.463984	A2764	29.53	25.04 ± 0.16	24.47 ± 0.08	23.95 ± 0.05	6.46	–
312245	5.758472	−49.460722	A2764	28.04	25.21 ± 0.18	24.27 ± 0.06	23.53 ± 0.03	5.69	1.56
316484	6.046452	−49.444592	A2764	27.95	25.32 ± 0.21	24.28 ± 0.07	23.49 ± 0.03	5.69	1.53
316921	5.318509	−49.443448	A2764	27.61	25.66 ± 0.30	24.53 ± 0.09	23.78 ± 0.04	5.69	1.69
317466	5.96933	−49.441346	A2764	28.47	25.66 ± 0.27	25.12 ± 0.14	24.29 ± 0.06	5.89	1.51
318092	6.127517	−49.439122	A2764	28.83	25.58 ± 0.25	24.59 ± 0.09	24.18 ± 0.06	7.17	–
331934	5.209565	−49.394328	A2764	27.38	25.12 ± 0.20	25.07 ± 0.16	24.20 ± 0.07	5.69	4.99
339812	5.754469	−49.37093	A2764	28.05	25.45 ± 0.25	24.25 ± 0.07	23.46 ± 0.03	5.69	1.69
342320	6.397808	−49.361065	A2764	27.73	25.36 ± 0.27	24.91 ± 0.14	24.34 ± 0.08	5.89	1.46
342359	5.594825	−49.363044	A2764	28.64	25.56 ± 0.25	23.98 ± 0.05	23.17 ± 0.02	7.17	1.80
349646	6.013694	−49.340953	A2764	27.89	25.36 ± 0.21	25.15 ± 0.14	24.75 ± 0.10	6.39	–
351918	6.383198	−49.332837	A2764	27.99	25.57 ± 0.28	25.15 ± 0.15	24.82 ± 0.11	6.03	1.46
352361	6.40128	−49.3315	A2764	27.85	25.71 ± 0.33	24.94 ± 0.13	24.14 ± 0.06	5.69	1.51
359339	5.498303	−49.313059	A2764	28.29	25.59 ± 0.26	25.25 ± 0.16	24.58 ± 0.09	5.96	1.51
361593	5.665488	−49.306737	A2764	28.93	25.61 ± 0.31	24.99 ± 0.15	24.36 ± 0.08	6.32	1.56
368096	5.982153	−49.287806	A2764	28.94	24.98 ± 0.14	24.32 ± 0.07	23.45 ± 0.03	5.96	–
368343	6.110498	−49.28676	A2764	28.15	25.52 ± 0.27	25.04 ± 0.14	24.06 ± 0.06	5.69	4.99
383133	5.998861	−49.246759	A2764	27.97	25.63 ± 0.27	25.07 ± 0.14	24.30 ± 0.07	5.62	1.51

Table B.4: Continued...

ID	RA [J2000]	Dec [J2000]	Field	I_E [mag]	Y_E [mag]	J_E [mag]	H_E [mag]	z_{phot}	$z_{phot}(< 5)$
388197	6.015296	−49.232755	A2764	28.02	25.22 ± 0.19	24.71 ± 0.10	23.80 ± 0.04	5.69	1.39
388530	5.711416	−49.232415	A2764	27.89	25.36 ± 0.20	24.67 ± 0.09	23.80 ± 0.04	5.62	1.44
399947	6.271704	−49.197094	A2764	28.30	25.54 ± 0.33	24.47 ± 0.10	23.44 ± 0.04	5.69	1.46
400268	5.034318	−49.195575	A2764	28.08	25.51 ± 0.27	24.68 ± 0.11	23.79 ± 0.05	5.69	1.46
409974	6.358018	−49.16543	A2764	27.23	24.87 ± 0.22	24.16 ± 0.09	23.64 ± 0.06	5.69	1.46
412279	6.074586	−49.159629	A2764	28.75	25.39 ± 0.21	24.71 ± 0.10	23.97 ± 0.05	6.10	–
412992	6.182453	−49.157207	A2764	27.94	25.69 ± 0.29	24.73 ± 0.10	24.19 ± 0.06	6.39	1.59
416453	6.134152	−49.147264	A2764	27.83	25.34 ± 0.21	24.48 ± 0.08	23.94 ± 0.05	5.69	1.56
417316	5.000542	−49.143334	A2764	27.62	25.32 ± 0.32	24.24 ± 0.10	23.59 ± 0.05	6.54	1.75
419641	5.32974	−49.137648	A2764	28.36	25.52 ± 0.23	24.89 ± 0.11	24.14 ± 0.05	6.03	1.53
429295	5.306015	−49.104542	A2764	28.12	25.55 ± 0.25	24.44 ± 0.07	23.89 ± 0.04	6.92	1.69
435610	5.503306	−49.083999	A2764	27.88	25.50 ± 0.24	24.66 ± 0.09	23.74 ± 0.04	5.69	1.44
444019	5.850835	−49.053654	A2764	28.38	24.81 ± 0.14	24.07 ± 0.06	23.32 ± 0.03	6.10	–
450433	5.935346	−49.028956	A2764	28.00	25.68 ± 0.26	24.82 ± 0.10	24.37 ± 0.07	6.32	1.53
461554	5.355018	−48.979285	A2764	28.02	24.93 ± 0.19	24.32 ± 0.09	23.47 ± 0.04	5.89	1.51
472651	5.910263	−48.926929	A2764	28.29	25.50 ± 0.29	24.14 ± 0.07	23.40 ± 0.03	7.08	1.92
474209	5.306756	−48.918358	A2764	27.90	24.75 ± 0.26	24.16 ± 0.13	23.79 ± 0.09	6.85	–
474659	5.359467	−48.915954	A2764	26.89	24.97 ± 0.33	24.59 ± 0.19	24.03 ± 0.11	5.69	1.39
482426	5.400998	−48.883814	A2764	27.35	24.39 ± 0.19	23.26 ± 0.06	22.55 ± 0.03	6.61	1.69
499104	5.756752	−48.719152	A2764	29.29	24.93 ± 0.26	24.23 ± 0.12	23.78 ± 0.07	6.85	–

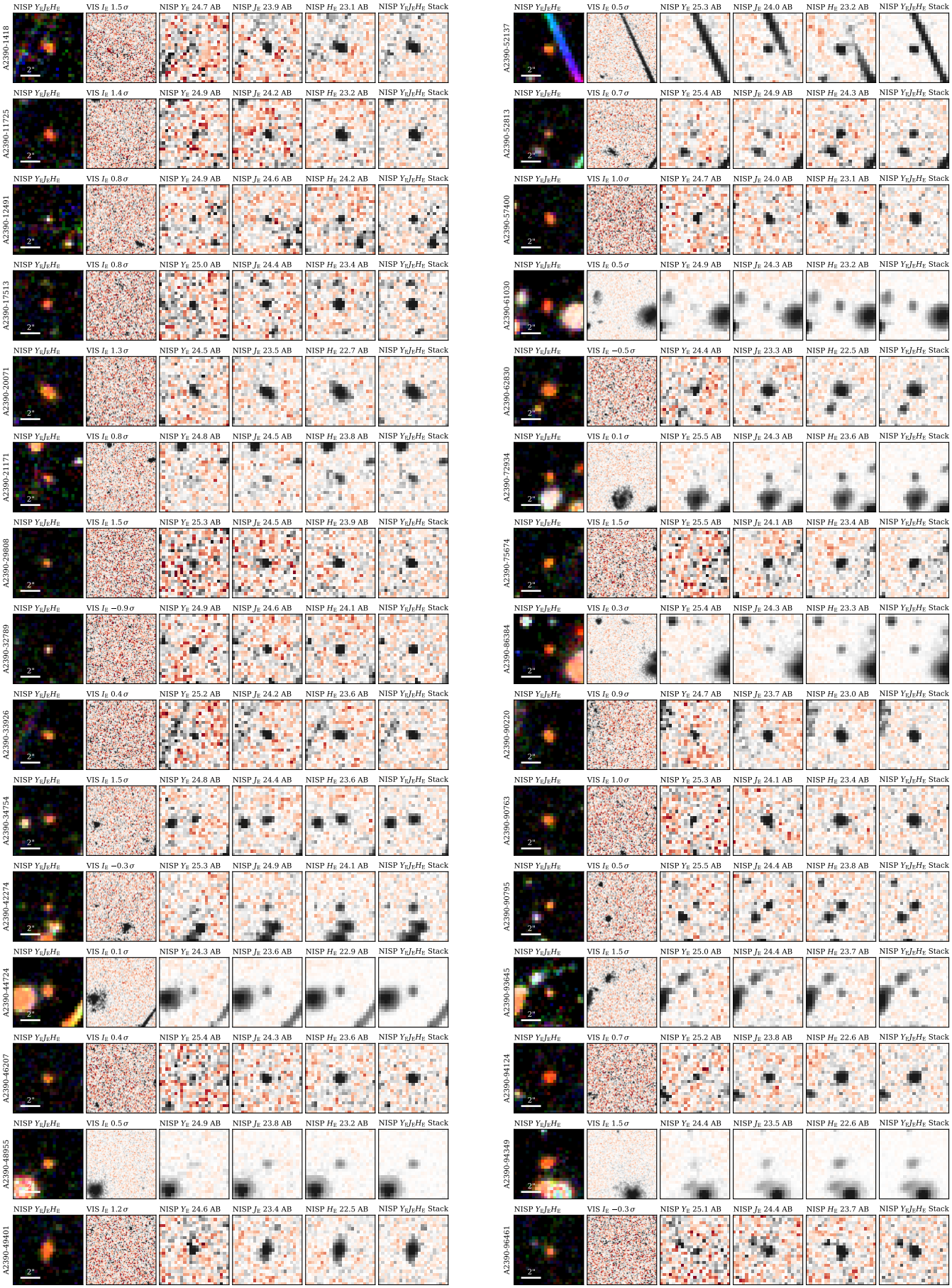

Fig. B.1: Cutouts of extremely red sources. Leftmost false-colour RBG images are constructed from NISP/Y_E, J_E, H_E. Others show VIS/I_E, NISP/Y_E, J_E, H_E, and the NISP detection stack, scaled to $\pm 3\sigma$ to emphasize the significance of the detections. Cutouts are 5″along a side.

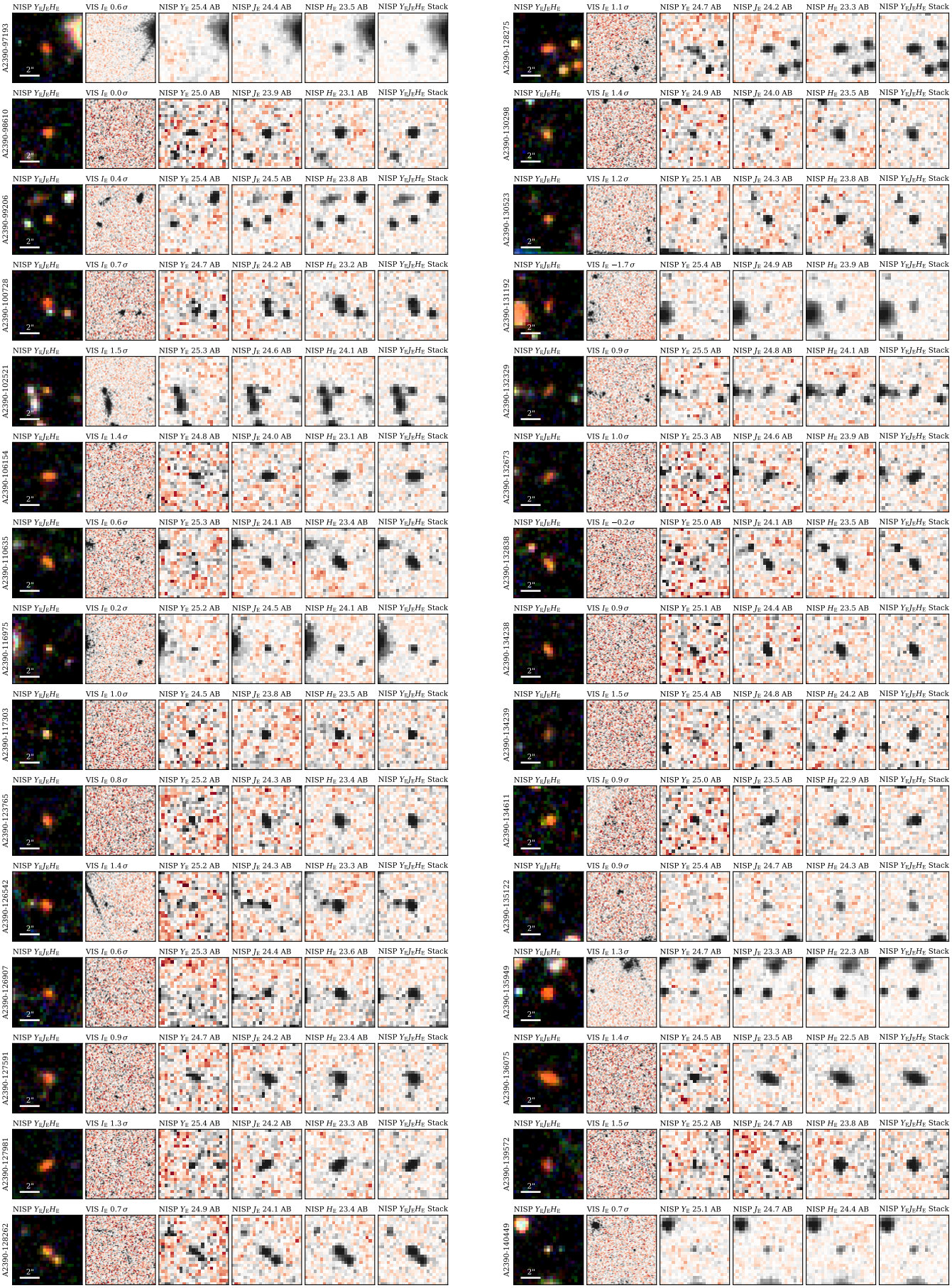

Fig. B.2: Continued...

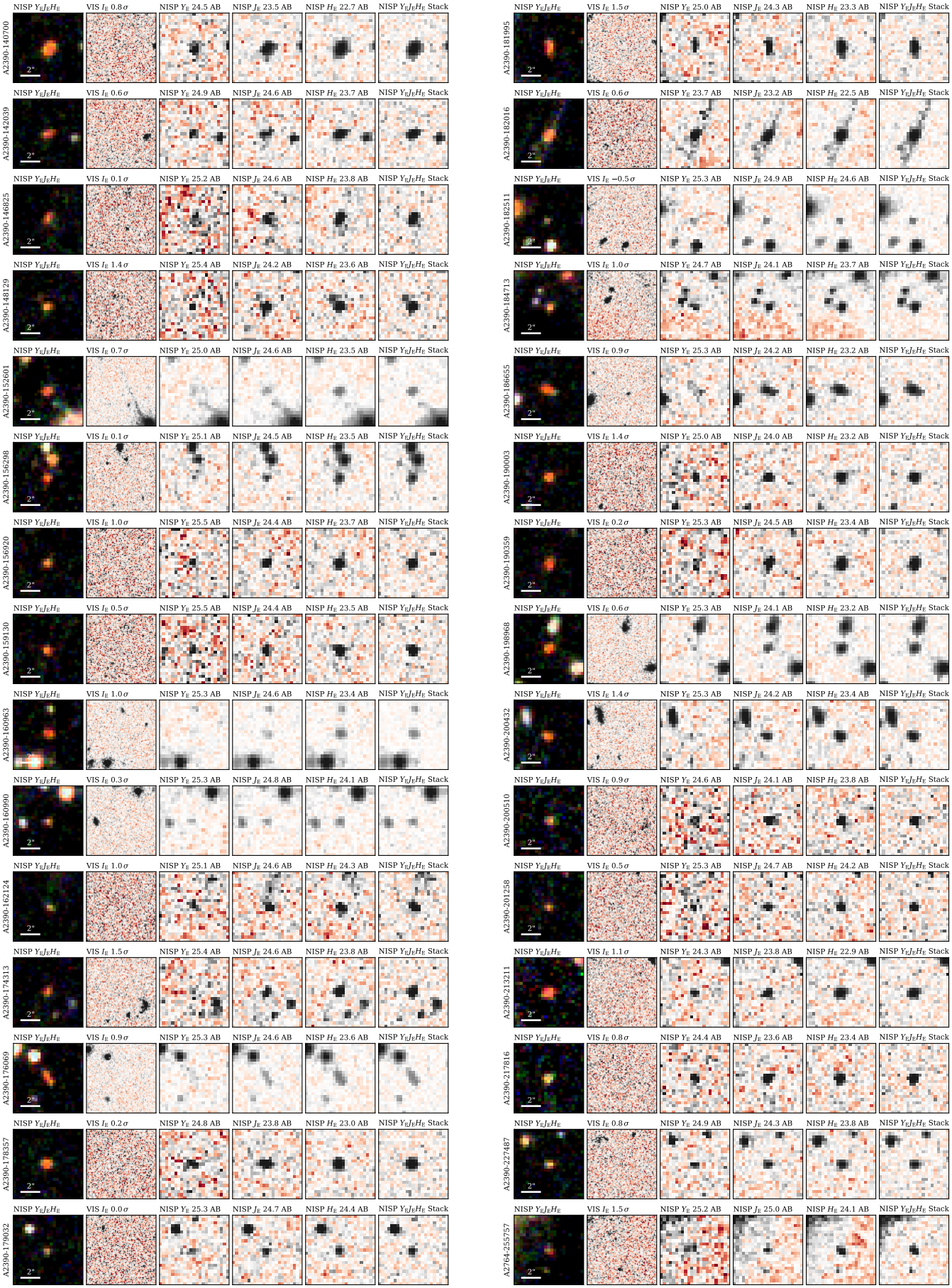

Fig. B.3: Continued...

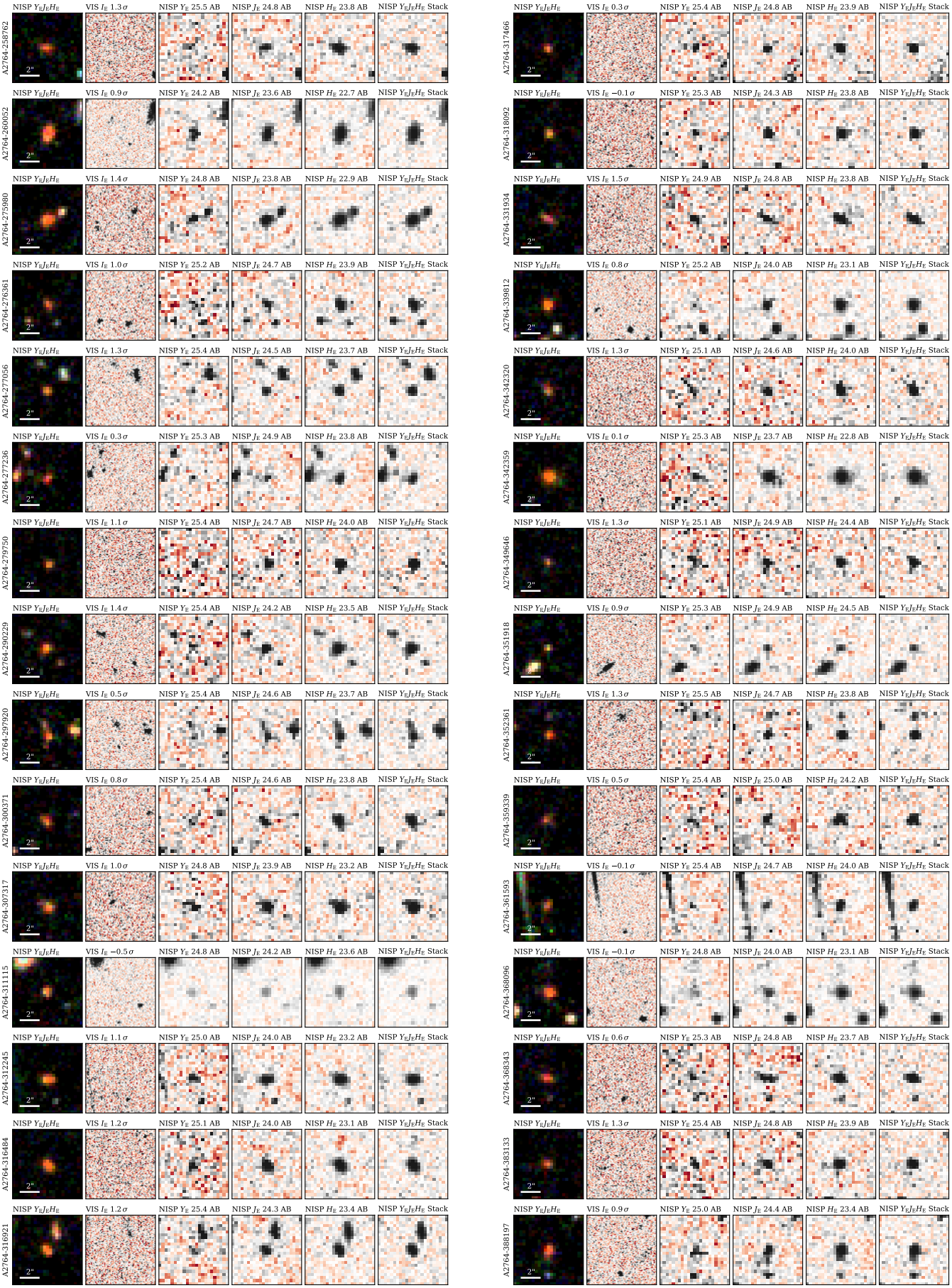

Fig. B.4: Continued...